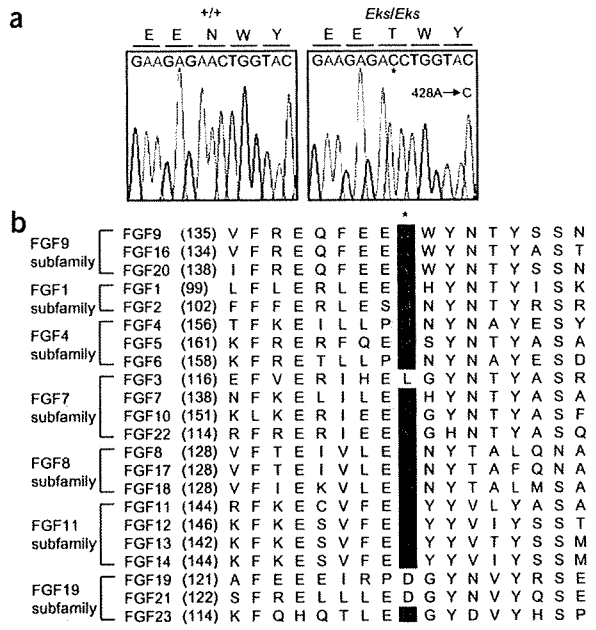

Figure 1 Missense mutation in the *Fgf9* gene of *Eks* mice. (**a**) Nucleotide sequence of the *Fgf9* cDNA derived from +/+ and *Eks*/*Eks* mice. *Eks* mutants have an A-to-C substitution at position 428, which results in the replacement of Asn143 with threonine. The *Eks* missense mutation is indicated by the asterisk, and the corresponding amino acid is shown in purple. (**b**) Structure-based sequence alignment of human FGFs. The amino acid sequence surrounding the N143T substitution in $FGF9^{Eks}$ and that of its corresponding domain in other human FGF family proteins are aligned on the basis of sequence identity. The Asn143 residue in FGF9 is highly conserved among most FGF proteins (purple box). The asterisk denotes the site of *Eks* mutation.

prevents homodimerization of FGF9, consequently decreasing the affinity of FGF9 for heparin. As a result, $FGF9^{Eks}$ is more diffusible in developing tissues, leading to ectopic FGF9 signaling in the prospective joints and sutures where it functions to repress development. Molecular-dynamics calculations suggest that the reduction in FGF9 affinity for heparin is due to the predominance of the monomeric form rather than to changes in its intrinsic affinity for heparin. We thus propose a mechanism in which the range of FGF9 signaling in developing tissues is limited through regulation of its affinity for HSPGs, which is at least in part controlled by the FGF9 monomer–dimer equilibrium. These observations could have far-reaching implications for the pharmacologic manipulation of FGF signaling under a variety of circumstances and in a wide range of tissues.

RESULTS

Eks is caused by a missense mutation in *Fgf9*

The *Eks* mutation was mapped between the polymorphic markers *D14Mit62* and *D14Mit5* on mouse chromosome 14 (ref. 16). Among 169 genes located in this interval, *Fgf9* seemed a likely candidate for the *Eks* mutation because FGF9 is a ligand for FGFR2c and FGFR3c[17] and is expressed in the developing limbs, cranial sutures and developing lung[8,18,19]. Sequence analysis of *Fgf9* cDNA from homozygous *Eks* mice revealed an A-to-C substitution at position 428, which resulted in the replacement of Asn143 with threonine (**Fig. 1a**). Notably, the Asn143 residue in FGF9 is highly conserved among most FGF proteins (**Fig. 1b**) and is predicted to be a critical amino acid residue for homodimerization and receptor binding[14,15].

We used a genetic approach to determine whether the N143T substitution in *Fgf9* was responsible for the *Eks* phenotype. We observed a mendelian pattern of inheritance of the mutation among 976 offspring of *Eks* heterozygous ($Fgf9^{Eks/+}$) matings, with heterozygous mice showing mild skeletal phenotypes and homozygous $Fgf9^{Eks/Eks}$ littermates showing severe skeletal phenotypes. The *Eks* phenotype and the mutation in *Fgf9* cosegregated in all cases. The absence of recombination between *Eks* and *Fgf9* among nearly 2,000 meiotic events provides strong evidence that the *Eks* mutation is allelic with *Fgf9*.

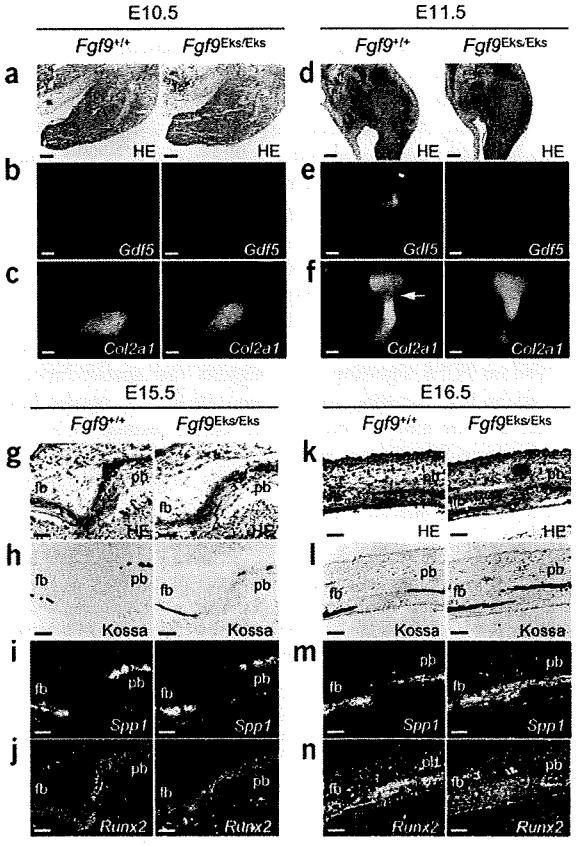

Figure 2 Synostotic phenotypes in $Fgf9^{Eks/Eks}$ mice. (**a–f**) Defects in early specification of prospective elbow joints in $Fgf9^{Eks/Eks}$ embryos. Hematoxylin and eosin staining (**a,d**) and *in situ* detection of *Gdf5* (**b,e**) and *Col2a1* (**c,f**) in the forelimb buds of $Fgf9^{+/+}$ and $Fgf9^{Eks/Eks}$ embryos at E10.5 and E11.5. In $Fgf9^{+/+}$ embryos, there was *Gdf5* expression at the prospective elbow joint (**e**, left), which was demarcated as the gap of *Col2a1* expression (**f**, arrow), at E11.5. In $Fgf9^{Eks/Eks}$ embryos, there was not *Gdf5* expression at the prospective elbow joint (**e**, right). Scale bars, 100 μm. (**g–n**) Ectopic osteogenesis at the coronal sutures in $Fgf9^{Eks/Eks}$ fetuses. Hematoxylin and eosin staining (**g,k**) and von Kossa staining (**h,l**) and *in situ* detection of *Spp1* (**i,m**) and *Runx2* (**j,n**) in the coronal suture of $Fgf9^{+/+}$ and $Fgf9^{Eks/Eks}$ fetuses at E15.5 and E16.5. Note the ectopic ossification in the suture of $Fgf9^{Eks/Eks}$ at E16.5. fb, frontal bone; pb, parietal bone. Scale bars, 100 μm.

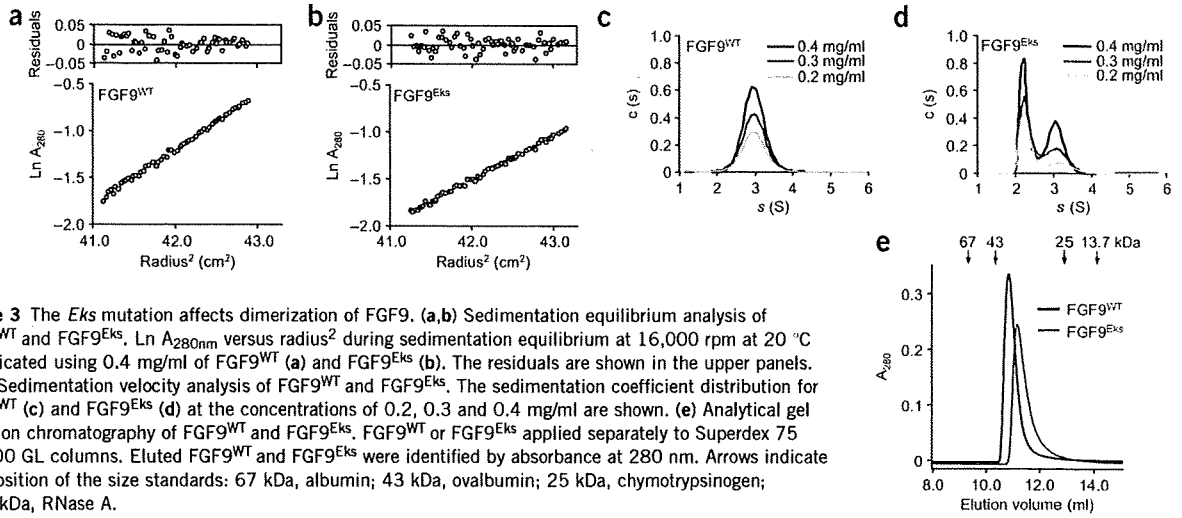

Figure 3 The *Eks* mutation affects dimerization of FGF9. (**a**,**b**) Sedimentation equilibrium analysis of $FGF9^{WT}$ and $FGF9^{Eks}$. Ln A_{280nm} versus radius^2 during sedimentation equilibrium at 16,000 rpm at 20 °C is indicated using 0.4 mg/ml of $FGF9^{WT}$ (**a**) and $FGF9^{Eks}$ (**b**). The residuals are shown in the upper panels. (**c**,**d**) Sedimentation velocity analysis of $FGF9^{WT}$ and $FGF9^{Eks}$. The sedimentation coefficient distribution for $FGF9^{WT}$ (**c**) and $FGF9^{Eks}$ (**d**) at the concentrations of 0.2, 0.3 and 0.4 mg/ml are shown. (**e**) Analytical gel filtration chromatography of $FGF9^{WT}$ and $FGF9^{Eks}$. $FGF9^{WT}$ or $FGF9^{Eks}$ applied separately to Superdex 75 10/300 GL columns. Eluted $FGF9^{WT}$ and $FGF9^{Eks}$ were identified by absorbance at 280 nm. Arrows indicate the position of the size standards: 67 kDa, albumin; 43 kDa, ovalbumin; 25 kDa, chymotrypsinogen; 13.7 kDa, RNase A.

Fgf9$^{Eks/Eks}$ mice phenocopy *Fgfr* gain-of-function mutants

Eks is a dominant mutation and joint synostosis and premature fusion of sutures have also been reported in mice expressing gain-of-function alleles of *Fgfr1* (ref. 20) and *Fgfr2c* (*Fgfr2*^{C342Y})[21]. Furthermore, homozygous *Fgf9* null mutants (*Fgf9*$^{-/-}$) show rhizomelia but not joint or suture synostosis[8]. Thus, we hypothesized that *Fgf9*^{Eks} encodes a gain-of-function mutation. To test this possibility, we first investigated whether there were phenotypic similarities between *Eks* mutants and gain-of-function mutants for *Fgfr1* and *Fgfr2*^{C342Y}. As initiation of elbow joint development was primarily impaired in *Fgfr1* gain-of-function transgenic mice[20], we examined radiohumeral joint development in *Fgf9*$^{Eks/Eks}$ mice (**Fig. 2a–f**). *Gdf5* (ref. 22) and *Col2a1* (ref. 23) demarcate the prospective elbow joint and cartilaginous condensation, respectively. *Gdf5* expression in the prospective joint space was observed as early as embryonic day E11.5 in *Fgf9*$^{+/+}$ control mice, but was completely absent in *Fgf9*$^{Eks/Eks}$ mice (**Fig. 2e**). Analysis of the prospective cartilage revealed a gap of *Col2a1* expression at the prospective elbow joint in E11.5 wild-type embryos (**Fig. 2f**, left). The gap of *Col2a1* expression was absent in *Fgf9*$^{Eks/Eks}$ mice (**Fig. 2f**, right). In summary, ectopic chondrocyte differentiation in the prospective elbow joint of *Fgf9*$^{Eks/Eks}$ mice seems very similar to that seen in transgenic mice that ectopically express an activated *Fgfr1* kinase domain in the presumptive joint field[20].

Premature fusion of coronal sutures in *Fgfr2*^{C342Y} mice results from excess osteogenic differentiation within the coronal suture mesenchyme[21]. To determine whether *Fgf9*$^{Eks/Eks}$ mice had similar histological features, we examined mineralization and the expression of the early osteoblast differentiation markers *Spp1* (ref. 24) and *Runx2* (ref. 25) in the coronal suture (**Fig. 2g–n**). At E15.5, both wild-type and *Fgf9*$^{Eks/Eks}$ mice showed similar coronal suture histology (**Fig. 2g–j**). However, at E16.5 von Kossa staining revealed considerably more overlap of the frontal and parietal bones in *Fgf9*$^{Eks/Eks}$ mice compared to *Fgf9*$^{+/+}$ mice (**Fig. 2l**). *Spp1* expression domains, which demarcate preosteoblasts and osteoblasts, showed wide separation of the frontal and parietal bones in *Fgf9*$^{+/+}$ mice; however, there was overlap in the *Fgf9*$^{Eks/Eks}$ mice (**Fig. 2m**). *Runx2* is highly expressed in immature osteoblasts at the leading edge of the frontal and parietal bones in *Fgf9*$^{+/+}$ mice (**Fig. 2n**, left). In E16.5 *Fgf9*$^{Eks/Eks}$ mice, the intensity of *Runx2* expression in the coronal suture was lower than in *Fgf9*$^{+/+}$ mice (**Fig. 2n**, right), suggesting premature differentiation of the osteoblasts at the presumptive suture. These phenotypes reflect abnormal osteogenic differentiation within the coronal suture mesenchyme and indicate that the defect in suture development occurs before E16.5. Taken together, these observations suggest that the $FGF9^{Eks}$ altered protein mediates excess FGFR signals within the prospective joints and sutures, preventing joint formation and promoting the fusion of cranial sutures.

The *Eks* mutation impairs homodimerization of FGF9

The predicted involvement of the Asn143 residue in homodimerization and receptor activation[14,15] suggests that changes in these processes may account for the apparent gain-of-function activity of the $FGF9^{Eks}$ altered protein. Homodimerization of FGF9 has been proposed to occlude receptor binding sites and consequently mediate an autoinhibitory mechanism for FGF9 signaling. We thus hypothesized that the *Eks* mutation might impair the autoinhibition. To test this possibility, we compared the degree of homodimerization of wild-type ($FGF9^{WT}$) and $FGF9^{Eks}$ proteins by analytical ultracentrifugation. $FGF9^{WT}$ and $FGF9^{Eks}$ were expressed in *Escherichia coli* and purified by column chromatography (**Supplementary Methods** and **Supplementary Fig. 2** online).

The molecular mass and association constant of $FGF9^{WT}$ and $FGF9^{Eks}$ were determined by sedimentation equilibrium centrifugation using the purified recombinant proteins (**Fig. 3a,b**). The estimated average molecular masses of $FGF9^{WT}$ and $FGF9^{Eks}$ were 39,264 and 32,929 Da, respectively, whereas the calculated monomeric molecular masses were 20,090 and 20,077 Da, respectively. These data suggest that $FGF9^{WT}$ primarily exists as a dimer, whereas $FGF9^{Eks}$ exists in a monomer–dimer equilibrium. The calculated association constants of $FGF9^{WT}$ and $FGF9^{Eks}$ were 10.4 μM^{-1} and 0.119 μM^{-1}, respectively. We further measured the sedimentation coefficient of $FGF9^{Eks}$ by sedimentation velocity centrifugation. The overlay plots of c(s)-sedimentation coefficient distributions show that $FGF9^{WT}$ has a unimodal peak at 3.0 S for a single ideal species, whereas $FGF9^{Eks}$ has bimodal peaks (2.2 S and 3.1 S) for two ideal species (**Fig. 3c,d**). This observation suggests that $FGF9^{WT}$ is present primarily as a dimer, whereas $FGF9^{Eks}$ exists primarily as a monomer. These interpretations are consistent with the retarded elution of $FGF9^{Eks}$

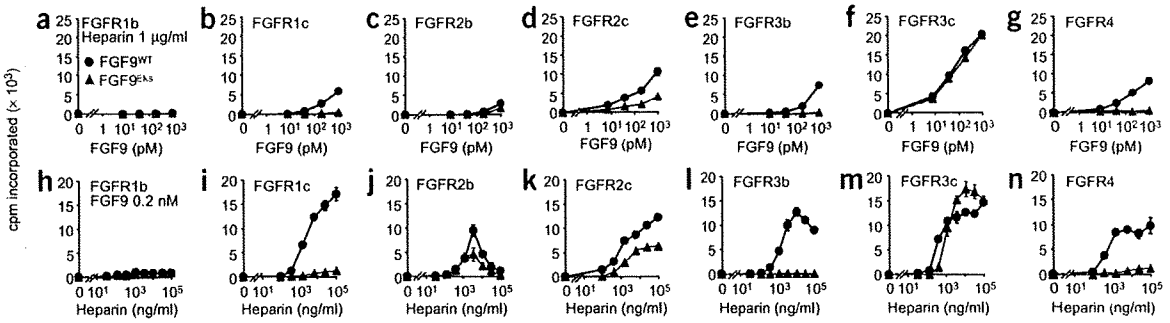

Figure 4 The *Eks* mutation affects the mitogenic activity of FGF9. (**a–g**) Dose-dependent changes in mitogenic activity of $FGF9^{WT}$ and $FGF9^{Eks}$. BaF3 cells expressing exogenous FGFR1b, 1c, 2b, 2c, 3b, 3c or 4 were treated with increasing concentrations of $FGF9^{WT}$ or $FGF9^{Eks}$ in the presence of 1 μg/ml heparin. Cell proliferation was determined by [^{3}H]thymidine incorporation after 36 h in culture. (**h–n**) Heparin-dependent changes in mitogenic activity of $FGF9^{WT}$ and $FGF9^{Eks}$. BaF3 cells expressing the respective FGFR were treated with increasing concentrations of heparin in the presence of 0.2 nM $FGF9^{WT}$ or $FGF9^{Eks}$. Cell proliferation was determined as above. Data are represented as mean ± s.e.m. of triplicate assays. These results are representative of at least two independent experiments.

relative to $FGF9^{WT}$ on a gel filtration column (**Fig. 3e**). Therefore, $FGF9^{Eks}$ is defective in homodimer formation.

$FGF9^{Eks}$ mediates less potent signaling via several FGFRs

To examine whether the *Eks* mutaion altered the binding of FGF9 to FGFRs by impairing the autoinhibitory mechanisms, we compared the ability of $FGF9^{WT}$ and $FGF9^{Eks}$ to activate FGFRs by assaying the mitogenic activity of both proteins on BaF3 cells expressing individual FGF receptors[17]. FGFR-expressing BaF3 cell lines were treated with increasing concentrations of purified recombinant FGF9 in the presence of 1 μg/ml heparin. Compared to $FGF9^{WT}$, $FGF9^{Eks}$ showed less activity on cells expressing any of the FGFRs except FGFR3c, where $FGF9^{Eks}$ showed equivalent activity (**Fig. 4a–g**). To test the ability of heparin to enhance FGF9 activity, we treated the BaF3 cell lines with increasing concentrations of heparin in the presence of 0.2 nM $FGF9^{WT}$ or $FGF9^{Eks}$. $FGF9^{Eks}$ also showed a decreased heparin-dependent mitotic response on all FGFRs except FGFR3c, where $FGF9^{Eks}$ showed higher activity in the presence of high concentrations of heparin (**Fig. 4h–n**). Because $FGF9^{Eks}$ does not mediate excess signaling via FGFRs, other properties of the altered protein must be responsible for the phenotype of the *Eks* mice.

The *Eks* mutation lowers FGF9 affinity for heparin

The decreased heparin-dependent mitogenic activity of $FGF9^{Eks}$ suggested that its affinity for heparin may be reduced. Heparin is functionally very similar to heparan sulfate, which is present in most tissues in the form of HSPGs. HSPGs function to modulate FGFR activation directly, by mediating FGF–FGFR interactions, and indirectly, by binding FGF ligands and regulating their diffusion through the extracellular matrix and thus their access to distant FGFRs[1,12,13,26]. As the gain-of-function property of $FGF9^{Eks}$ may not involve direct interaction with the FGFRs, we hypothesized that its decreased affinity for heparin might allow increased diffusion and thus bioavailability in

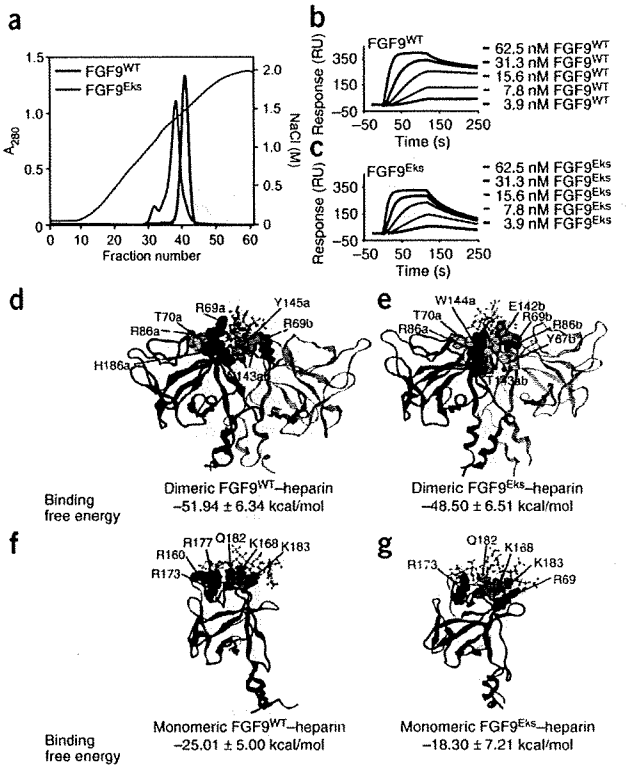

Figure 5 The *Eks* mutation reduces FGF9 affinity for heparin by impairing its dimerization. (**a**) Chromatographic analysis of the affinities of $FGF9^{WT}$ and $FGF9^{Eks}$ for heparin. $FGF9^{WT}$ or $FGF9^{Eks}$ were loaded onto a heparin-conjugated agarose column and eluted with a linear gradient of NaCl from 120 mM to 2.0 M (black line). Elution profiles of $FGF9^{WT}$ and $FGF9^{Eks}$ were determined by monitoring absorbance at 280 nm. (**b,c**) Surface plasmon resonance analysis of the affinities of $FGF9^{WT}$ and $FGF9^{Eks}$ for heparin. Sensorgrams indicating the interaction of $FGF9^{WT}$ (**b**) and $FGF9^{Eks}$ (**c**) with immobilized heparin were determined at different concentrations. The biosensor chip response is indicated on the *y* axis (RU) as a function of time (*x* axis) at room temperature. (**d–g**) The most probable solution structures of dimeric $FGF9^{WT}$–heparin (**d**), dimeric $FGF9^{Eks}$–heparin (**e**), monomeric $FGF9^{WT}$–heparin (**f**) and monomeric $FGF9^{Eks}$–heparin (**g**) complexes deduced by molecular-dynamics simulations. Heparin and protein residues that form important hydrogen bonds are drawn in ball and stick and space-filling modes. The single-letter amino acid code, residue number and chain code are indicated for each of these residues. Computed binding free energy of each complex is shown under the respective illustrated structure. Data are represented as mean ± s.d. of energies obtained from 200 molecular-dynamics snapshots in respective molecular-dynamics trajectory.

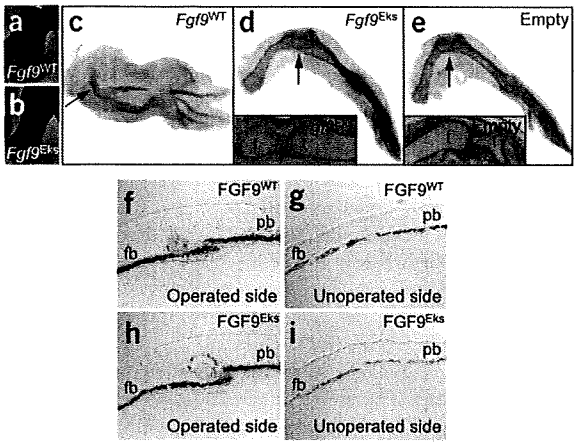

Figure 6 $FGF9^{Eks}$ can inhibit joint and suture development as well as $FGF9^{WT}$. (**a–e**) Inhibition of knee joint development induced by ectopic expression of $Fgf9^{WT}$ and $Fgf9^{Eks}$. Hindlimb buds of Hamburger-Hamilton stage 17 chickens were infected with RCAS-$Fgf9^{WT}$, RCAS-$Fgf9^{Eks}$ or empty RCAS virus. (**a,b**) *Fgf9* expression was examined by *in situ* hybridization 2 d after infection. (**c–e**) Respective knee joints (arrows) were examined by Alcian blue staining and hematoxylin and eosin staining of sections through the knee joint (insets in **d** and **e**) 5 d after infection. f, femur; t, tibia. (**f–i**) Inhibition of coronal suture development by the ectopic presence of $FGF9^{WT}$ and $FGF9^{Eks}$. $FGF9^{WT}$ or $FGF9^{Eks}$ beads were implanted onto the coronal suture in E15 mice, and the *Spp1* expression was examined by *in situ* hybridization 24 h after implantation. On the operated sides with $FGF9^{WT}$ (**f**) and $FGF9^{Eks}$ (**h**) bead implants, there was overlap of *Spp1* expression in the frontal and parietal bones, which was not seen on the unoperated sides (**g,i**). fb, frontal bone; pb, parietal bone.

tissues. To address this possibility, we first measured FGF9–heparin affinity by heparin affinity chromatography (**Fig. 5a**). $FGF9^{WT}$ was eluted from heparin-conjugated agarose with 1.50 M NaCl as a single peak. In contrast, most $FGF9^{Eks}$ was eluted at 1.38 M NaCl and a small fraction eluted at 1.10 M NaCl.

We next measured the kinetic constants for the $FGF9^{Eks}$–heparin interaction using surface plasmon resonance analysis (**Fig. 5b,c** and **Supplementary Table 1** online). The resulting sensorgrams were used for kinetic parameter determination by globally fitting the experimental data to a 1:1 interaction model. The association rate constant (k_a) of $FGF9^{Eks}$ was slightly greater than that of $FGF9^{WT}$, whereas the dissociation rate constant (k_d) of $FGF9^{Eks}$ was 18-fold greater than that of $FGF9^{WT}$. The dissociation constants (K_D) for $FGF9^{WT}$ and $FGF9^{Eks}$ were 0.71 ± 0.02 nM and 5.24 ± 0.03 nM, respectively, representing an 86% decrease in affinity of the $FGF9^{Eks}$ protein for heparin.

Dimerization of FGF9 confers heparin affinity

The above studies indicate the $Fgf9^{Eks}$ mutation concurrently affects monomer–dimer equilibrium and affinity for heparin. We thus went on to address whether the N143T substitution directly affects the affinity of FGF9 for heparin or whether it directly affects homodimerization and secondarily affects heparin affinity. However, direct biochemical measurements of the affinity of the two species for heparin are not possible because monomeric and dimeric forms of FGF9 are in equilibrium. We therefore analyzed the configuration of heparin-binding domains in monomeric and dimeric FGF9 using molecular-dynamics simulations and calculated the binding free energy between FGF9 and heparin using the molecular mechanics Poisson-Boltzmann/surface area (MM-PBSA) method. It is well known that the binding free energies calculated by this method show good qualitative but not quantitative agreement with experimental observations[27].

To model the heparin binding affinity of FGF9, we carried out molecular-dynamics simulations of 2:2 $FGF9^{WT}$–heparin and 2:2 $FGF9^{Eks}$–heparin complexes based on a 2:2:2 FGF2-FGFR1-heparin crystal structure (Protein Data Bank (PDB) ID: 1FQ9)[28]. The conformations of two heparin oligosaccharides in each complex were influenced by strong electrostatic repulsions, resulting in the exclusion of one heparin oligosaccharide from the complex (data not shown). This analysis suggested that 2:2 FGF9–heparin complexes would be unstable. In contrast, molecular-dynamics simulations of 2:1 $FGF9^{WT}$–heparin, 2:1 $FGF9^{Eks}$–heparin, 1:1 $FGF9^{WT}$–heparin and 1:1 $FGF9^{Eks}$–heparin complexes suggested that these complexes are stable (**Fig. 5d–g**). Molecular-dynamics simulations of dimeric FGF9–heparin complexes did not show a big difference in heparin-binding free energies for 2:1 $FGF9^{WT}$–heparin (dimeric $FGF9^{WT}$–heparin) and 2:1 $FGF9^{Eks}$–heparin (dimeric $FGF9^{Eks}$–heparin) complexes (**Fig. 5d,e**). This is due to the strong interaction between the negatively charged heparin oligosaccharide chain and the array of basic amino acid residues located in the heparin binding site near the groove of the dimer interface in both dimeric complexes. In addition, flexibility of the heparin oligosaccharide chain would help to maintain electrostatic interactions. Similarly, there was little difference in the heparin-binding free energies in 1:1 $FGF9^{WT}$–heparin (monomeric $FGF9^{WT}$–heparin) and 1:1 $FGF9^{Eks}$–heparin (monomeric $FGF9^{Eks}$–heparin) complexes (**Fig. 5f,g**). This is also due to heparin oligosaccharide chain flexibility, the strong negative charge of the heparin oligosaccharide and the presence of several basic amino acid residues in the heparin binding site. Therefore, the *Eks* mutation does not seem to influence the heparin binding affinity of either the dimeric or the monomeric FGF9–heparin complex. Because the heparin-binding free energies for dimeric FGF9 (**Fig. 5d,e**) were smaller than those for monomeric FGF9–heparin for both $FGF9^{WT}$ and $FGF9^{Eks}$ (**Fig. 5f,g**), the reduced binding affinity to heparin of the $FGF9^{Eks}$ protein is most likely due to the shift in the monomer–dimer equilibrium toward the monomer. In summary, the *Eks* mutation primarily affects homodimerization of FGF9 and only secondarily affects heparin affinity.

$FGF9^{Eks}$ is potentially hyperdiffusible in tissues

Heparin–FGF2 interactions have previously been shown to regulate the diffusibility of FGF2 (refs. 26,29). We hypothesized that the diffusibility of $FGF9^{Eks}$ in tissues would be increased because of its lower affinity for heparin, leading to ectopic localization outside of the normal signaling domain and, consequently, ectopic activation of FGFRs. However, this model can only be considered if the following two prerequisites are met: first, *Fgf9* and *Fgfrs* are expressed in the proximity of the prospective elbow and knee joints and coronal sutures and, second, the increased diffusibility of $FGF9^{Eks}$ is dominant over its decreased ability to activate FGFRs.

We first examined the expression of *Fgf9* and *Fgfr1*, *Fgfr2* and *Fgfr3* in the forelimb buds in E10.5 and E11.5 mice. *Fgf9* was expressed in migrating myoblasts, both in $Fgf9^{+/+}$ and $Fgf9^{Eks/Eks}$ mice (**Supplementary Fig. 3a,b,i,j** online). At E10.5, *Fgfr1*, *Fgfr2* and *Fgfr3* were expressed diffusely in the limb bud mesenchyme, overlapping the expression domain of *Col2a1* in both $Fgf9^{+/+}$ and $Fgf9^{Eks/Eks}$ tissues (**Supplementary Fig. 3c–h**). At E11.5, *Fgfr1* expression was excluded from the cartilaginous condensation, whereas *Fgfr2* and *Fgfr3*

expression was observed mainly in this location (**Supplementary Fig. 3k–p**). Therefore, mesenchymal cells in the prospective elbow joint express FGFRs.

Previous reports showed that *Fgf9* is expressed in the developing frontal and parietal bones, particularly strongly at the rims of the bones[18]. *Fgfr1*, *Fgfr2* and *Fgfr3* are expressed within and around the developing frontal and parietal bone domains[30]. Thus, the first prerequisite was validated.

FGF9^{Eks} is able to inhibit joint and suture development

To address the second prerequisite for our model, we examined the inhibitory effects of FGF9^{WT} and FGF9^{Eks} on joint development by ectopically expressing them in the chicken limb bud using a replication component retroviral vector (RCAS) transduction. RCAS-*Fgf9*^{WT}, RCAS-*Fgf9*^{Eks} or empty RCAS virus was used to infect the prospective hindlimb bud region in the lateral plate mesoderm. FGF9^{WT} and FGF9^{Eks} were expressed throughout the hindlimb buds (**Fig. 6a,b**). Ectopic expression of both *Fgf9*^{WT} and *Fgf9*^{Eks} caused knee joint fusion (**Fig. 6c,d**), whereas no abnormalities were induced by the empty vector (**Fig. 6e**). Therefore, FGF9^{Eks} retains inhibitory effects on joint development as well as FGF9^{WT}. It is notable that skeletal defects induced by the expression of FGF9^{WT} were widespread, whereas those mediated by FGF9^{Eks} were limited to the prospective joint regions. This is consistent with our finding that FGF9^{Eks} preferentially activates FGFR3c (**Fig. 4**), which is expressed in the bone anlagen (**Supplementary Fig. 3**), whereas FGF9^{WT} is expected to activate all of the mesodermally expressed FGFRs.

To examine the inhibitory effects of FGF9^{WT} and FGF9^{Eks} on suture development, we implanted FGF9-soaked AffiGel-Blue beads in the coronal suture of normal mouse fetal skulls around the initiation stage of the suture defect, at E15, by *ex utero* surgery. We first confirmed that approximately equal amounts of FGF9^{WT} and FGF9^{Eks} were loaded in each AffiGel-Blue bead and that the diffusion rates of FGF9^{WT} and FGF9^{Eks} from the beads were almost identical (**Supplementary Fig. 4** online). The expression of *Spp1*, an early osteoblast differentiation marker upregulated by FGF9, was examined 24 h after *in utero* bead placement. Grafts of FGF9^{WT} and FGF9^{Eks} beads also promoted ectopic *Spp1* expression at the leading edges of the frontal and parietal bones (**Fig. 6f–i**). This FGF9-induced ectopic expression of *Spp1* resembled that observed in the *Fgf9*$^{Eks/Eks}$ coronal suture (**Fig. 2m**, right). Therefore, ectopic expression of either FGF9^{Eks} or FGF9^{WT} within the suture inhibits suture development.

FGF9^{Eks} is more diffusible than FGF9^{WT} in developing tissues

To examine whether the diffusibility of FGF9^{Eks} in mesenchymal tissue is increased in comparison with FGF9^{WT}, we measured the diffusibility of FGF9^{WT} and FGF9^{Eks} in the skull following bead implantation (**Fig. 7a–e**). Because FGF9 upregulates *Spp1* expression, we could measure the area of high *Spp1* expression as an indication of

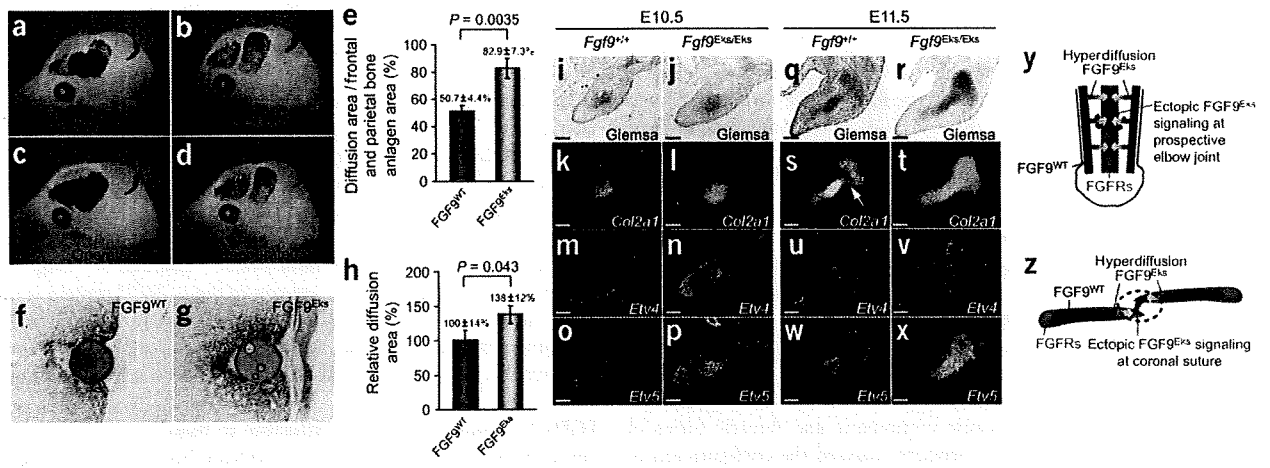

Figure 7 Ectopic FGF9^{Eks} signaling due to its hyperdiffusibility. (**a–e**) Increased diffusibility of FGF9^{Eks} in the skull bone anlagen. FGF9^{WT} or FGF9^{Eks} beads were implanted onto the coronal suture at E15 mice and *Spp1* expression was examined by whole-mount *in situ* hybridization 24 h after implantation. On the operated sides with FGF9^{WT} (**a**) and FGF9^{Eks} (**c**) bead implants, we observed well-defined intense signals in the frontal and parietal bone anlagen around the implants, which were not seen on the unoperated side (**b,d**). This domain with intense *Spp1* signals reflects diffusibility of exogenous FGF9 proteins. We therefore compared diffusibility of FGF9^{WT} and FGF9^{Eks} based on the induced expression domain of *Spp1* (**e**). The diffusion areas (%) in the frontal and parietal bone anlagen area were estimated from the area ratio of the intense *Spp1* expression against the frontal and parietal bone anlagen. Data are represented as mean ± s.e.m. of six operations. FGF9^{Eks} is more diffusible than FGF9^{WT}. Significance was determined by two-tailed Student's *t*-test. (**f–h**) Increased diffusibility of FGF9^{Eks} in the forelimb bud. FGF9^{WT} or FGF9^{Eks} beads were implanted into forelimb buds of *Fgf9*$^{-/-}$ embryos of E10.5 mice. Diffusion of exogenous FGF9^{WT} (**f**) and FGF9^{Eks} (**g**) after 2 h was immunodetected using a FGF9 antibody. (**h**) The diffusion area of FGF9^{Eks} and FGF9^{WT} was measured at the level of the equator of the beads. Data are represented as mean (FGF9^{WT} = 100%) ± s.e.m. of four (FGF9^{WT}) or five (FGF9^{Eks}) operations. FGF9^{Eks} is also more diffusible than FGF9^{WT} in limb buds. Significance was determined by one-tailed Student's *t*-test. (**i–x**) The downstream target genes of FGF signaling, *Etv4* and *Etv5*, are expressed ectopically in the prospective elbow joint in *Fgf9*$^{Eks/Eks}$ mice. Counterstaining with Giemsa (**i,j,q,r**) and *in situ* detection of *Col2a1* (**k,l,s,t**), *Etv4* (**m,n,u,v**) and *Etv5* (**o,p,w,x**) in the forelimb buds of *Fgf9*$^{+/+}$ and *Fgf9*$^{Eks/Eks}$ embryos at E10.5 and E11.5. There was ectopic expression of *Etv4* (**n,v**) and *Etv5* (**p,x**), in the cartilaginous condensation including the prospective elbow joint position, which was demarcated as the gap of *Col2a1* expression (**s**, arrow), in *Fgf9*$^{Eks/Eks}$, which were not seen in *Fgf9*$^{+/+}$ mice (**m,o,u,w**). Scale bars, 100 μm. (**y**) A model for the pathogenic mechanism underlying elbow joint synosotsis in *Fgf9*$^{Eks/Eks}$ mice. In *Fgf9*$^{Eks/Eks}$ mice, ectopic FGF9 signaling due to hyperdiffusion of FGF9^{Eks} at the prospective elbow joint may inhibit the initiation of joint development. (**z**) A model for the pathogenic mechanism underlying premature fusion of the coronal suture in *Fgf9*$^{Eks/Eks}$ mice. In *Fgf9*$^{Eks/Eks}$ mice, ectopic FGF9 signaling due to hyperdiffusion of FGF9^{Eks} at the coronal suture may promote ectopic osteogenesis and subsequently induce premature fusion of the suture.

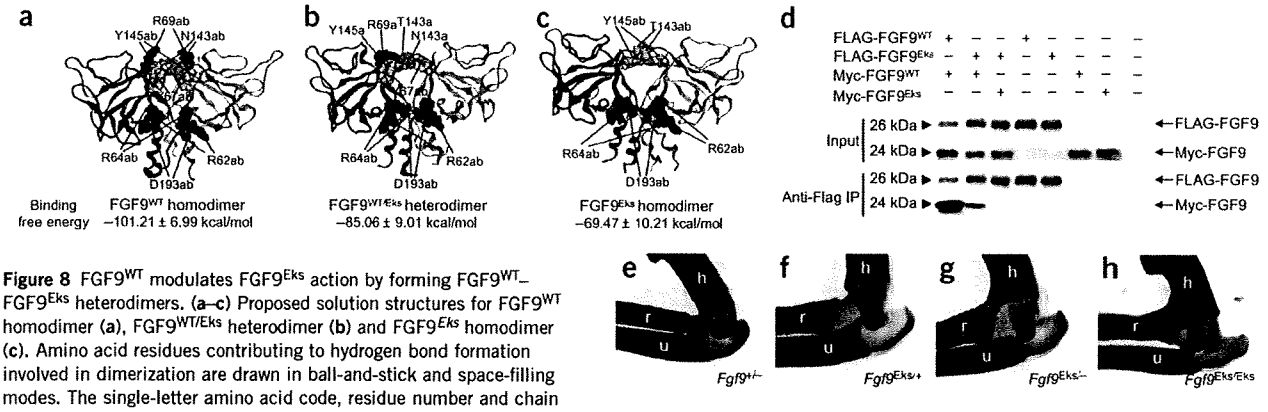

Figure 8 $FGF9^{WT}$ modulates $FGF9^{Eks}$ action by forming $FGF9^{WT}$–$FGF9^{Eks}$ heterodimers. (**a–c**) Proposed solution structures for $FGF9^{WT}$ homodimer (**a**), $FGF9^{WT/Eks}$ heterodimer (**b**) and $FGF9^{Eks}$ homodimer (**c**). Amino acid residues contributing to hydrogen bond formation involved in dimerization are drawn in ball-and-stick and space-filling modes. The single-letter amino acid code, residue number and chain code are indicated for each of these residues. Computed binding free energy of each dimer is shown under the respective illustrated structure. Data are represented as mean ± s.d. of energies obtained from 200 molecular-dynamics snapshots in respective molecular-dynamics trajectory. (**d**) $FGF9^{WT}$ is capable of forming dimers with $FGF9^{Eks}$. The expression of $FGF9^{WT}$ homodimers, $FGF9^{WT/Eks}$ heterodimers and $FGF9^{Eks}$ homodimers was analyzed using immunoprecipitation and protein blots. The expression vectors for FLAG- or Myc-tagged $FGF9^{WT}$ and $FGF9^{Eks}$ were transfected into COS7 cells and culture supernatants were subjected to immunoprecipitation and protein blot analysis. (**e–h**) Less severe elbow joint synostosis in $Fgf9^{Eks/+}$ than $Fgf9^{Eks/-}$. Forelimbs from $Fgf9^{+/-}$, $Fgf9^{Eks/+}$, $Fgf9^{Eks/-}$ and $Fgf9^{Eks/Eks}$ embryos at E17.5 were stained with Alcian blue and Alizarin red. Synostotic change is restricted to the cartilaginous component in $Fgf9^{Eks/+}$ embryos, whereas it is extended to the bony component in $Fgf9^{Eks/-}$ and $Fgf9^{Eks/Eks}$ embryos. h, humerus; r, radius; u, ulna.

the distance over which FGF9 exerts its effects. Implantation of $FGF9^{Eks}$ beads resulted in a larger area of *Spp1* expression (high *Spp1* expression area / Frontal and parietal bone anlagen area = 82.9 ± 7.3%) (± s.e.m.) compared with beads loaded with $FGF9^{WT}$ (50.7 ± 4.4%; $P = 0.0035$), suggesting that the altered protein diffused more effectively through the developing tissue.

Next, we investigated the diffusibility of $FGF9^{Eks}$ in forelimb buds. $FGF9^{WT}$- or $FGF9^{Eks}$-soaked AffiGel-Blue beads were grafted into the dorsal and central forelimb bud region of $Fgf9^{-/-}$ embryos around the initiation stage of the joint defect, at E10.5. FGF9 protein released from the beads into mesenchymal tissue 2 h after implantation was detected by immunohistochemistry using FGF9 antibodies on sections (**Fig. 7f–h**). This analysis showed that $FGF9^{Eks}$ permeated through the limb bud mesenchyme to a greater extent (relative disffusion area = 138 ± 12%) (± s.e.m.) than $FGF9^{WT}$ (100 ± 14%; $P = 0.043$), supporting the hypothesis that $FGF9^{Eks}$ is more diffusible than $FGF9^{WT}$.

Ectopic FGF signaling in the prospective joint of *Eks* mice

To examine whether diffusion of endogenous $FGF9^{Eks}$ is increased in comparison to $FGF9^{WT}$, we determined the degree of activation of FGFRs in the prospective elbow joint of $Fgf9^{Eks/Eks}$ mice. As a readout for FGFR signaling, we examined the expression of *Etv4* and *Etv5*, both of which are known to be transcriptionally activated by FGF signaling, in the forelimb buds[31] (**Fig. 7i–x**). In wild-type E10.5 limbs, we did not observe the intensive expression of *Etv4* or *Etv5* within the region undergoing cartilaginous condensation demarcated by *Col2a1* expression (**Fig. 7m,o**). However, in E10.5 $Fgf9^{Eks/Eks}$ limbs, we found ectopic expression of both *Etv4* and *Etv5* in the cartilaginous condensation (**Fig. 7n,p**). At E11.5, *Etv4* and *Etv5* were expressed in the myoblasts and cells surrounding the cartilaginous condensation in wild-type mice (**Fig. 7u,w**), whereas in $Fgf9^{Eks/Eks}$ mice, we observed clear expression of *Etv4* and *Etv5* in the cartilaginous condensation including the prospective elbow joint position (**Fig. 7v,x**). These results demonstrate ectopic FGF signaling in the prospective elbow joint in $Fgf9^{Eks/Eks}$ mice. Because the ectopic expression domain of *Etv4* and *Etv5* in $Fgf9^{Eks/Eks}$ mice was not consistent with the *Fgf9* expression domain (**Supplementary Fig. 3a,b,i,j**), this outcome is likely due to increased diffusion of $FGF9^{Eks}$ protein over a larger area than $FGF9^{WT}$.

From these results, we propose a mechanism of elbow joint synostosis in $Fgf9^{Eks/Eks}$ mice in which $FGF9^{Eks}$ produced by myoblasts diffuses beyond its normal range and ectopically activates FGFRs in the prospective elbow joint, preventing joint formation (**Fig. 7y**). Similarly, $FGF9^{Eks}$ produced at the rims of the frontal and parietal bones diffuses beyond its normal area and ectopically activates FGFRs in the coronal suture mesenchyme, promoting the fusion of coronal sutures (**Fig. 7z**).

Genetic validation of the hyperdiffusible model

A prediction of our model is that the severity of synostotic phenotypes will correlate with a shift in the equilibrium of FGF9 from dimer toward monomer. By molecular-dynamics simulations, we estimated that $FGF9^{WT}$ homodimer, $FGF9^{WT/Eks}$ heterodimer and $FGF9^{Eks}$ homodimer have ten, eight, six intermonomer hydrogen bonds, respectively (**Fig. 8a–c** and **Supplementary Table 2** online). From these results, we calculated the binding free energy of the $FGF9^{WT/Eks}$ heterodimer to be between those of the $FGF9^{WT}$ and $FGF9^{Eks}$ homodimers (**Fig. 8a–c**), suggesting that $FGF9^{WT/Eks}$ heterodimers are more stable than $FGF9^{Eks}$ homodimers. If our model is correct, $FGF9^{WT}$ should interfere with $FGF9^{Eks}$ action by forming $FGF9^{WT/Eks}$ heterodimers. In other words, skeletal phenotypes due to the *Eks* mutation should be alleviated by the expression of $FGF9^{WT}$.

We first sought experimental evidence that the $FGF9^{WT/Eks}$ heterodimer was substantially more stable than the $FGF9^{Eks}$ homodimer. We addressed this issue by immunoprecipitation and protein blot analysis after tagging $FGF9^{WT}$ and $FGF9^{Eks}$ with Flag or Myc peptides. Flag-$FGF9^{WT}$ or Flag-$FGF9^{Eks}$ was overexpressed together with Myc-$FGF9^{WT}$ or Myc-$FGF9^{Eks}$ in COS7 cells and the culture supernatants were subjected to the immunoprecipitation and protein blot analysis (**Fig. 8d**). We readily detected Flag-$FGF9^{WT}$–Myc-$FGF9^{WT}$ dimers. Flag-$FGF9^{Eks}$–Myc-$FGF9^{WT}$ dimers were detected at lower level; however, Flag-$FGF9^{Eks}$–Myc-$FGF9^{Eks}$

dimers did not form under these conditions. These data suggest that $FGF9^{WT}$ and $FGF9^{Eks}$ can form heterodimers that are more stable than $FGF9^{Eks}$ homodimers.

We finally examined whether the elbow synostosis caused by $FGF9^{Eks}$ could be alleviated by the expression of $FGF9^{WT}$. We thus compared the severity of elbow synostosis in $Fgf9^{Eks/+}$ and compound heterozygous mutants ($Fgf9^{Eks/-}$) relative to that of $Fgf9^{+/-}$ and $Fgf9^{Eks/Eks}$ mice (**Fig. 8e–h**). Elbow joint formation was not affected in $Fgf9^{+/-}$ mice (**Fig. 8e**), whereas elbow synostosis in $Fgf9^{Eks/Eks}$ mice involved both cartilaginous and bony components (**Fig. 8h**). In contrast, the synostosis in $Fgf9^{Eks/+}$ mice was limited to the cartilaginous component (**Fig. 8f**), whereas the involvement of the bony component in $Fgf9^{Eks/-}$ mice was similar to that of $Fgf9^{Eks/Eks}$ mice (**Fig. 8g**). Therefore, elbow synostosis in $Fgf9^{Eks/-}$ is more severe than in $Fgf9^{Eks/+}$. These findings strongly support our model that the monomer–dimer status of FGF9 influences its affinity for HSPGs and, consequently, its distribution in developing tissues.

DISCUSSION

In the present study, we identified a missense mutation in the *Fgf9* gene that is responsible for the *Eks* mutant phenotype, which includes elbow and knee joint synostosis and craniosynostosis. We further demonstrate that the N143T substitution in FGF9 favors formation of the monomeric form of FGF9, which binds to heparin with a lower affinity than dimeric FGF9. The decreased affinity for heparin leads to increased diffusion of the altered protein in developing tissues, resulting in ectopic FGF9 signaling. We propose that regulation of the monomer–dimer equilibrium of FGF9, and potentially of other FGFs, and its affinity for HSPGs is a mechanism that functions to shape FGF9 concentration gradients in developing tissues. We further propose that these biochemical properties of FGF9 restrict its signaling activity to limited skeletal domains. Data presented here and in previous studies indicate that low FGF signaling in the presumptive joint space is necessary for the formation of the joint space and maintenance of an open suture[20,21]. Common usage of receptor binding and homodimerization sites of FGF9 could be at least in part instrumental for local modulation of FGF9 signaling activity.

Homodimerization is suggested to be a common feature of the FGF9/16/20 subfamily[32] and of FGF2 (refs. 33,34). It is not known to what extent homodimerization affects the activity of other FGFs. The discovery that a mutation in *Fgf9* can affect homodimerization, affinity for heparin and biological activity suggests that pharmacological agents that affect FGF homodimerization could be useful tools to modulate its activity.

METHODS

Detection of a mutation in the *Fgf9* gene. To identify the mutation responsible for the *Eks* mutant phenotype, we surveyed the cDNA sequence of *Fgf9* from normal (+/+), heterozygous (*Eks*/+) and homozygous (*Eks/Eks*) mice through reverse transcription-PCR (RT-PCR) and direct sequencing of RT-PCR products.

For genotyping of the *Eks* allele, genomic DNA spanning the *Eks* mutation was amplified by PCR using specific primers (**Supplementary Table 3** online). PCR products were digested with the diagnostic *Bsr*I restriction enzyme. Wild-type mice show two bands of 147 bp and 42 bp, whereas the *Eks* allele shows one band of 189 bp (**Supplementary Fig. 5** online).

Skeletal and histological preparations. Bones and cartilage of E17.5 fetuses were stained with Alizarin red and Alcian blue as previously described[35]. For histological preparations, tissues were fixed in 4% paraformaldehyde, embedded in paraffin, sectioned at 5 μm, and stained with hematoxylin and eosin and von Kossa.

***In situ* hybridization.** *In situ* hybridization of paraffin sections was done as previously described[36], using radiolabeled antisense RNA for *Gdf5* (MGI: 95688), *Col2a1* (MGI: 88452), *Spp1* (MGI: 98389), *Runx2* (MGI: 99829), *Fgf9* (MGI: 104723), *Fgfr1* (MGI: 95522), *Fgfr2* (MGI: 95523), *Fgfr3* (MGI: 95524), *Etv4* (MGI: 99423) and *Etv5* (MGI: 1096867). *In situ* hybridization after bead implantation in fetal skulls was done as previously described[24].

$FGF9^{WT}$ and $FGF9^{Eks}$ expression and purification. $FGF9^{WT}$ and $FGF9^{Eks}$ expression and purification were done as described in **Supplementary Methods.**

Analytical ultracentrifugation. All analytical ultracentrifuge experiments were done on a Beckman Coulter XL-I analytical ultracentrifuge. We diluted the samples in 25 mM ammonium acetate buffer (pH 5.5) containing 120 mM NaCl. The partial specific volumes were estimated as 0.7317 ml/g ($FGF9^{WT}$) or 0.7322 ml/g ($FGF9^{Eks}$) by SEDNTERP software. All experiments were done at 20 °C and the absorbance wavelength was 280 nm. We carried out sedimentation equilibrium experiments with six channel centerpieces, with loading concentrations of 0.8, 0.4 and 0.2 mg/ml. Data were obtained at 12, 14 and 16 k rpm for $FGF9^{WT}$ or at 14, 16 and 18 k rpm for $FGF9^{Eks}$. A total equilibration time of 16 h was used for each speed with scans taken at 12, 14 and 16 h. We analyzed the sedimentation equilibrium data using the Beckman XL-A/XL-I Data Analysis software. All nine datasets (three speeds, three concentrations) were fitted together by 'self association model' calculation. Sedimentation velocity experiments were carried out with double sector centerpieces. Protein concentrations were 0.4, 0.3 or 0.2 mg/ml. We scanned the absorbance data 100 times every 5 min at 40 k rpm. The measurements data were analyzed by SEDFIT software.

Analytical gel filtration chromatography. Purified $FGF9^{WT}$ and $FGF9^{Eks}$ (100 μl of 2 mg/ml) were loaded onto a Superdex75 10/300 GL column (GE Healthcare) equilibrated with a 25 mM ammonium acetate buffer (pH 5.5) containing 120 mM NaCl. The samples were eluted with the same buffer.

Mitogenic assays. The ability of $FGF9^{WT}$ and $FGF9^{Eks}$ to transduce signals via FGFRs was analyzed by a mitogenic assay using BaF3 cells expressing specific FGFRs as described previously[17]. We plated 5,000 cells per well in a 96-well assay plate in media containing varying concentrations of FGF9 and heparin (Wako). $FGF9^{WT}$ or $FGF9^{Eks}$ were added to each well for a total volume of 200 μl per well. The cells were then incubated at 37 °C for 36 h. We added 1 μCi of [^{3}H]thymidine to each well in 20 μl of media. The cells were harvested after 4 h by filtration through glass fiber paper and the incorporated [^{3}H]thymidine was counted on a Wallac MicroBeta TriLux scintillation counter (PerkinElmer).

Analytical heparin affinity chromatography. We loaded 3 mg of purified $FGF9^{WT}$ and $FGF9^{Eks}$ onto a 1 ml HiTrap heparin HP column (GE Healthcare) equilibrated with 25 mM ammonium acetate buffer (pH 5.5) containing 120 mM NaCl. The bound $FGF9^{WT}$ or $FGF9^{Eks}$ were eluted with a linear gradient of NaCl (120 mM to 2.0 M) in the same buffer.

Surface plasmon resonance analysis of FGF9–heparin interactions. Surface plasmon resonance analysis for measurements of $FGF9^{WT}$–heparin and $FGF9^{Eks}$–heparin interactions were done using a BIAcore 3000 instrument (Biacore AB). In order to immobilize heparin (Wako) on the streptavidin-conjugated sensor chip SA, 100 μg/ml biotinylated heparin in HBS-EP buffer was injected at a flow rate of 10 μl/min and was immobilized to 63 response units (RU). All measurements were carried out at room temperature, and refractive index errors due to bulk solvent effects were corrected by subtracting responses on the noncoated sensor chip for the $FGF9^{WT}$ and $FGF9^{Eks}$ concentrations used. To obtain kinetic data, we injected different concentrations of analytes ($FGF9^{WT}$ and $FGF9^{Eks}$) in HBS-EP over the heparin sensor chip at a flow rate of 20 μl/min. At the end of each sample injection (120 s), HBS-EP buffer was passed over the sensor surface to monitor the dissociation phase. Following 120 s of dissociation, the sensor surface was regenerated by injection of 5 μl of 1 M NaCl in HBS-EP. We used five different analyte concentrations to determine the kinetic parameters for each interaction. Kinetic parameters were obtained by global fitting of the sensorgrams to a 1:1 model using BIAevaluation software.

Molecular-dynamics simulation. Starting structures of monomeric $FGF9^{WT}$, dimeric $FGF9^{WT}$, monomeric $FGF9^{WT}$-heparin, dimeric $FGF9^{WT}$-heparin and $FGF9^{Eks}$ for molecular-dynamics simulations were taken from the PDB (PDB ID: 1IHK)[14]. The structures of monomeric $FGF9^{Eks}$, dimeric $FGF9^{Eks}$ and heterodimeric $FGF9^{WT/Eks}$ were constructed based on $FGF9^{WT}$ using molecular modeling software MOE (Chemical Computing Group). A hexasasaccharide (UAP-SGN-IDU-SGN-IDU-SGN) is used as a heparin oligosaccharide. UAP is 1,4-dideoxy-5-dehydro-O2-sulfo-glucuronic acid, SGN is O6-disulfo-glucosamin and IDU is 1,4-dideoxy-O2-sulfo-glucuronic acid. For monomeric $FGF9^{WT}$–heparin and dimeric $FGF9^{WT}$–heparin simulations, heparin oligosaccharide was bound to $FGF9^{WT}$ structures obtained from molecular-dynamics simulations using the molecular docking program GOLD (version 3.0)[37]. In the docking protocol, the standard default setting of GA parameters was used and GoldScore was used as the scoring function. The structures of monomeric $FGF9^{Eks}$–heparin and dimeric $FGF9^{Eks}$–heparin were built in the same manner as $FGF9^{WT}$–heparin complexes. All the starting structures for molecular-dynamics simulations were surrounded by TIP3P water molecules[38] spherically. After energy minimizations, all molecular-dynamics simulations were carried out for 10 ns at 300 K using modified Amber 8.0 (ref. 39) for MDGRAPE3 system[40]. The Amber ff03 force field[41] was adopted, and the simulation time step was set at 1 s. We calculated the binding free energies by the molecular mechanics Poisson-Boltzmann/surface area (MM-PBSA) method[42] using the last 2 ns molecular-dynamics trajectories.

Retroviral misexpression. Mouse $Fgf9^{WT}$ and $Fgf9^{Eks}$ cDNAs were cloned into the RCASBP(A) vector[43]. The virus solutions were injected into the hind limb bud of chicken embryos at Hamburger-Hamilton stage 17. We examined the expression of mouse *Fgf9* transcripts and skeletal changes 2 and 5 d after injection, respectively.

Subcutaneous insertion of $FGF9^{Eks}$ beads in mouse fetal skulls. AffiGel-Blue beads (BioRad) soaked in 100 μg/ml $FGF9^{WT}$ or $FGF9^{Eks}$ were implanted onto E15 mouse skulls by *ex utero* surgery as previously described[24] Operated heads were collected 24 h later and *Spp1* transcripts were detected by whole-mount *in situ* hybridization. The area of *Spp1* expression was measured using NIH image software.

Implantation of $FGF9^{Eks}$ beads in mouse forelimb buds. AffiGel-Blue beads that had been soaked in 500 μg/ml $FGF9^{WT}$ or $FGF9^{Eks}$ were implanted into the dorsal and central region of E10.5 $Fgf9^{-/-}$ forelimb buds. Limb buds were subsequently cultured for 2 h on Transwell filters (Costar, Coaning) in serum-free medium (BGJb, 2 mg/ml BSA, penicillin (50 units/ml), streptomycin (50 μg/ml)), in a humid, 37 °C and 5% CO_2 environment. Explants were fixed in 4% paraformaldehyde and embedded in paraffin. Sections through the equator of the bead were analyzed for exogenous FGF9 using goat antibody to FGF9 (R&D Systems) and a cell and tissue staining kit HRP-AEC system (R&D Systems). We analyzed the signal area and intensity using NIH image software.

Immunoprecipitation and protein blot analysis. cDNA fragments encoding the full length mouse $FGF9^{WT}$ and $FGF9^{Eks}$ proteins were cloned into the p3xFlag-CMV-14 vector (Sigma-Aldrich) and into the pCMV-Tag3B vector (Stratagene) to allow expression of FGF9 proteins with either C-terminal Myc or 3xFlag tags. These vectors were transfected into COS7 cells, and 48 h later, culture supernatants were incubated with anti-Flag M2 affinity beads (Sigma-Aldrich) for 1 h at RT and washed three times with PBS and then subjected to protein blots with antibody to Flag M2 (Sigma-Aldrich) or antibody to Myc (Upstate).

Note: Supplementary information is available on the Nature Genetics website.

ACKNOWLEDGMENTS

This study was supported in part by the RIKEN Structural Genomics/Proteomics Initiative (RSGI) and the National Project on Protein Structural and Functional Analysis, Ministry of Education, Culture, Sports, Science and Technology of Japan (S.Y.) and US National Institutes of Health grant HD049808 (D.M.O.).

AUTHOR CONTRIBUTIONS

M.H., D.M.O. and H.K. developed the project and wrote the manuscript. M.H., S.H. and H.K. contributed to the purification of FGF9 proteins, mitogenic assays, analytical gel filtration chromatography, analytical heparin affinity chromatography, surface plasmon resonance analysis, skeletal preparation, histological analyses and *in situ* hybridization of sections, implantation of FGF9 beads in mouse forelimb buds and immunoprecipitation and protein blot analysis. H.M., A.O. and H.K. contributed to the identification of the *Eks* mutation. N.O., N.F. and M.T. contributed to the molecular-dynamics simulation. T.N. and S.I. contributed to the implantation of FGF9 beads in mouse fetal skulls. R.A., M.S. and S.Y. contributed to the analytical ultracentrifugation. Y.S. and A.K. contributed to the retroviral misexpression. Y.M.-K. contributed to the *in situ* hybridization of sections.

Published online at http://www.nature.com/naturegenetics/
Reprints and permissions information is available online at http://npg.nature.com/reprintsandpermissions/

1. Ornitz, D.M. & Itoh, N. Fibroblast growth factors. *Genome Biol.* **2**, reviews 3005 (2001).
2. Wilkie, A.O.M. Bad bone, absent smell, selfish testes: the pleiotropic consequences of human FGF receptor mutations. *Cytokine Growth Factor Rev.* **16**, 187–203 (2005).
3. Su, N., Du, X. & Chen, L. FGF signaling: its role in bone development and human skeleton diseases. *Front. Biosci.* **13**, 2842–2865 (2008).
4. Ornitz, D.M. & Marie, P.J. FGF signaling pathways in endochondral and intramembranous bone development and human genetic disease. *Genes Dev.* **16**, 1446–1465 (2002).
5. Martin, G.R. The roles of FGFs in the early development of vertebrate limbs. *Genes Dev.* **12**, 1571–1586 (1998).
6. Ornitz, D.M. FGF signaling in the developing endochondral skeleton. *Cytokine Growth Factor Rev.* **16**, 205–213 (2005).
7. Montero, A. *et al.* Disruption of the fibroblast growth factor-2 gene results in decreased bone mass and bone formation. *J. Clin. Invest.* **105**, 1085–1093 (2000).
8. Hung, I.H., Yu, K., Lavine, K.J. & Ornitz, D.M. FGF9 regulates early hypertrophic chondrocyte differentiation and skeketal vascularization in the developing stylopod. *Dev. Biol.* **307**, 300–313 (2007).
9. Liu, Z., Xu, J., Colvin, J.S. & Ornitz, D.M. Coordination of chondrogenesis and osteogenesis by fibroblast growth factor 18. *Genes Dev.* **16**, 859–869 (2002).
10. Ohbayashi, N. *et al.* FGF18 is required for normal cell proliferation and differentiation during osteogenesis and chondrogenesis. *Genes Dev.* **16**, 870–879 (2002).
11. Garofalo, S. *et al.* Skeletal dysplasia and defective chondrocyte differentiation by targeted overexpression of fibroblast growth factor 9 in transgenic mice. *J. Bone Miner. Res.* **14**, 1909–1915 (1999).
12. Ornitz, D.M. FGFs, heparan sulfate and FGFRs: complex interactions essential for development. *Bioessays* **22**, 108–112 (2000).
13. Nybakken, K. & Perrimon, N. Heparan sulfate proteoglycan modulation of developmental signaling in *Drosophila*. *Biochim. Biophys. Acta* **1573**, 280–291 (2002).
14. Plotnikov, A.N. *et al.* Crystal structure of fibroblast growth factor 9 reveals regions implicated in dimerization and autoinhibition. *J. Biol. Chem.* **276**, 4322–4329 (2001).
15. Hecht, H.J. *et al.* Structure of fibroblast growth factor 9 shows a symmetric dimer with unique receptor- and heparin-binding interfaces. *Acta Crystallogr. D Biol. Crystallogr.* **57**, 378–384 (2001).
16. Murakami, H. *et al.* Elbow knee synostosis (Eks): a new mutation on mouse Chromosome 14. *Mamm. Genome* **13**, 341–344 (2002).
17. Ornitz, D.M. *et al.* Receptor specificity of the fibroblast growth factor family. *J. Biol. Chem.* **271**, 15292–15297 (1996).
18. Hajihosseini, M.K. & Heath, J.K. Expression patterns of fibroblast growth factors-18 and -20 in mouse embryos is suggestive of novel roles in calvarial and limb development. *Mech. Dev.* **113**, 79–83 (2002).
19. Colvin, J.S., Feldman, B., Nadeau, J.H., Goldfarb, M. & Ornitz, D.M. Genomic organization and embryonic expression of the mouse fibroblast growth factor 9 gene. *Dev. Dyn.* **216**, 72–88 (1999).
20. Wang, Q., Green, R.P., Zhao, G. & Ornitz, D.M. Differential regulation of endochondral bone growth and joint development by FGFR1 and FGFR3 tyrosine kinase domains. *Development* **128**, 3867–3876 (2001).
21. Eswarakumar, V.P., Horowitz, M.C., Locklin, R., Morriss-Kay, G.M. & Lonai, P. A gain-of-function mutation of *Fgfr2c* demonstrates the roles of this receptor variant in osteogenesis. *Proc. Natl. Acad. Sci. USA* **101**, 12555–12560 (2004).
22. Storm, E.E. & Kingsley, D.M. Joint patterning defects caused by single and double mutations in members of the bone morphogenetic protein (BMP) family. *Development* **122**, 3969–3979 (1996).
23. Nalin, A.M., Greenlee, T.K. & Sandell, L.J. Collagen gene expression during development of avian synovial joints: Transient expression of types II and XI collagen genes in the joint capsule. *Dev. Dyn.* **203**, 352–362 (1995).
24. Iseki, S. *et al. Fgfr2* and *osteopontin* domains in the developing skull vault are mutually exclusive and can be altered by locally applied FGF2. *Development* **124**, 3375–3384 (1997).

25. Yoshida, T. *et al.* Twist is required for establishment of the mouse coronal suture. *J. Anat.* **206**, 437–444 (2005).
26. Flaumenhaft, R., Moscatelli, D. & Rifkin, D.B. Heparin and heparan sulfate increase the radius of diffusion and action of basic fibroblast growth factor. *J. Cell Biol.* **111**, 1651–1659 (1990).
27. Woo, H.J. & Roux, B. Calculation of absolute protein-ligand binding free energy from computer simulations. *Proc. Natl. Acad. Sci. USA* **102**, 6825–6830 (2005).
28. Schlessinger, J. *et al.* Crystal structure of a ternary FGF-FGFR-heparin complex reveals a dual role for heparin in FGFR binding and dimerization. *Mol. Cell* **6**, 743–750 (2000).
29. Dowd, C.J., Cooney, C.L. & Nugent, M.A. Heparan sulfate mediates bFGF transport through basement membrane by diffusion with rapid reversible binding. *J. Biol. Chem.* **274**, 5236–5244 (1999).
30. Johnson, D., Iseki, S., Wilkie, A.O.M. & Morriss-Kay, G.M. Expression patterns of Twist and *Fgfr1, -2* and *-3* in the developing mouse coronal suture suggest a key role for Twist in suture initiation and biogenesis. *Mech. Dev.* **91**, 341–345 (2000).
31. Tsang, M. & Dawid, I.B. Promotion and attenuation of FGF signaling through the Ras–MAPK pathway. *Sci. STKE* **2004**, pe17 (2004).
32. Mohammadi, M., Olsen, S.K. & Ibrahimi, O.A. Structural basis for fibroblast growth factor receptor activation. *Cytokine Growth Factor Rev.* **16**, 107–137 (2005).
33. Ornitz, D.M. *et al.* Heparin is required for cell-free binding of basic fibroblast growth factor to a soluble receptor and for mitogenesis in whole cells. *Mol. Cell. Biol.* **12**, 240–247 (1992).
34. Venkataraman, G., Shriver, Z., Davis, J.C. & Sasisekharan, R. Fibroblast growth factors 1 and 2 are distinct in oligomerization in the presence of heparin-like glycosaminoglycans. *Proc. Natl. Acad. Sci. USA* **96**, 1892–1897 (1999).
35. Kessel, M. & Gruss, P. Murine developmental control genes. *Science* **249**, 374–379 (1990).
36. Kessel, M. & Gruss, P. Homeotic transformations of murine vertebrae and concomitant alteration of Hox codes induced by retinoic acid. *Cell* **67**, 89–104 (1991).
37. Verdonk, M.L., Cole, J.C., Hartshorn, M.J., Murray, C.W. & Taylor, R.D. Improved protein-ligand docking using GOLD. *Proteins* **52**, 609–623 (2003).
38. Jorgensen, W.L., Chandrasekhar, J., Madura, J.D., Impey, R.W. & Klein, M.L. Comparison of simple potential functions for simulating liquid water. *J. Chem. Phys.* **79**, 926–935 (1983).
39. Case, D.A. *et al. AMBER 8* (University of California, San Francisco, 2004).
40. Narumi, T. *et al.* A 55 Tflops simulation of amyloid-forming peptides from yeast prion Sup35 with the special-purpose computer System MD-GRAPE3. <http://doi.acm.org/10.1145/1188455.1188506> (2006).
41. Duan, Y. *et al.* A point-charge force field for molecular mechanics simulations of proteins based on condensed-phase quantum mechanical calculations. *J. Comput. Chem.* **24**, 1999–2012 (2003).
42. Srinivasan, J., Miller, J., Kollma, P.A. & Case, D.A. Continuum solvent studies of the stability of RNA hairpin loops and helices. *J. Biomol. Struct. Dyn.* **16**, 671–682 (1998).
43. Hughes, S.H., Greenhouse, J.J., Petropoulos, C.J. & Sutrave, P. Adaptor plasmids simplify the insertion of foreign DNA into helper-independent retroviral vectors. *J. Virol.* **61**, 3004–3012 (1987).

The EMBO Journal (2009), 1–15 | © 2009 European Molecular Biology Organization | All Rights Reserved 0261-4189/09
www.embojournal.org

THE EMBO JOURNAL

MAPKAP kinase MK2 maintains self-renewal capacity of haematopoietic stem cells

Jessica Schwermann[1,4], Chozhavendan Rathinam[2,4,5], Maria Schubert[1,4], Stefanie Schumacher[1], Fatih Noyan[2], Haruhiko Koseki[3], Alexey Kotlyarov[1,4], Christoph Klein[2,4] and Matthias Gaestel[1,4,*]

[1]Institute of Biochemistry, Hannover Medical School, Hannover, Germany, [2]Department of Pediatric Hematology/Oncology, Hannover Medical School, Hannover, Germany and [3]RIKEN Research Center for Allergy and Immunology, Tsurumi-ku, Yokohama, Japan

The structurally related MAPK-activated protein kinases (MAPKAPKs or MKs) MK2, MK3 and MK5 are involved in multiple cellular functions, including cell-cycle control and cellular differentiation. Here, we show that after deregulation of cell-cycle progression, haematopoietic stem cells (HSCs) in MK2-deficient mice are reduced in number and show an impaired ability for competitive repopulation *in vivo*. To understand the underlying molecular mechanism, we dissected the role of MK2 in association with the polycomb group complex (PcG) and generated a MK2 mutant, which is no longer able to bind to PcG. The reduced ability for repopulation is rescued by re-introduction of MK2, but not by the Edr2-non-binding mutant of MK2. Thus, MK2 emerges as a regulator of HSC homeostasis, which could act through chromatin remodelling by the PcG complex.

The EMBO Journal advance online publication, 16 April 2009; doi:10.1038/emboj.2009.100

Subject Categories: signal transduction; differentiation & death

Keywords: chromatin remodelling; haematopoiesis; mouse knockout; protein kinase

Introduction

Haematopoietic stem cells (HSCs) represent the best-characterized type of adult stem cells. Profound analysis of surface antigens and established protocols to determine the self-renewal capacity and differentiation make HSCs a favourite model for stem cell biology. The complex microenvironment in the bone marrow regulates the fate of HSCs, controlling the balance between differentiation and self-renewal by providing cytokine and growth factors. However, intracellular signalling pathways involved in HSCs maintenance remain elusive. Recent studies showed controversial roles of evolutionarily conserved signalling pathways such as Smad-, Notch- and Wingless/Int(Wnt)-type (Reya *et al*, 2003; Duncan *et al*, 2005; Blank *et al*, 2006). The p38 mitogen-activated protein kinase (MAPK) pathway mainly regulates haematopoiesis by myelosuppressive cytokines that inhibit the growth of human primitive haematopoietic progenitors (reviewed in Platanias, 2003). p38 MAPK was also described to be necessary for erythropoietin expression and erythropoiesis (Tamura *et al*, 2000) and for thrombopoietin-induced self-renewal and expansion of HSCs through homeobox protein Hoxb4 (Kirito *et al*, 2003). More recently, the involvement of p38 MAPK in oxidative stress-elicited HSC depletion was shown (Ito *et al*, 2006). However, redundancy in these signalling pathways as well as the early embryonic lethality of most knockout mouse models makes the systemic analysis of the involvement of these pathways still puzzling.

The three MAPKAP kinases (MKs), MK2, MK3 and MK5, are involved in the regulation of inflammatory-cytokine production, in rearrangement of the cytoskeleton and cell migration, in cell-cycle checkpoint control, in developmental regulation, as well as in chromatin repression and remodelling (reviewed in Gaestel, 2006). Whereas the regulatory function of MKs in cytokine production is well known (Kotlyarov *et al*, 1999; Winzen *et al*, 1999), their role in controlling chromatin repression and remodelling remains elusive. Recent evidence indicates that polycomb group proteins may be targets for MK2 (Yannoni *et al*, 2004) and MK3 (Voncken *et al*, 2005). The polycomb group family, originally identified in *Drosophila melanogaster* as a repressor of homeotic genes, represents epigenetic chromatin modifiers with transcriptional silencing function (Zink and Paro, 1989; Valk-Lingbeek *et al*, 2004). In *Drosophila* and mammals, two cooperating PcG complexes have been identified (Lund and van Lohuizen, 2004). The polycomb repressive or initiation complex (PRC2), which shows histone-modifying activity, cooperates with the polycomb maintenance complex (PRC1), which interacts with modified histones to repress the expression of genes (Levine *et al*, 2004), such as the developmental regulators in murine embryonic stem cells (Boyer *et al*, 2006). In humans, PRC1 is a multiprotein complex including the human polycomb proteins HPC1–3, core proteins such as RING1A, RING1B, BMI1, as well as the early development regulator/human polyhomeotic EDR1/HPH1 and EDR2/HPH2. PcG proteins can interact with a series of additional molecules to exert control on gene expression in a highly regulated and dynamic manner (reviewed in Lund and van Lohuizen, 2004).

A crucial role of PRC1 and its individual components has been shown by analysis of mice with targeted deletion of mouse homologues of BMI1 (Bmi1), EDR1/HPH1 (Edr1/Mph1/Phc1/Rae28) and EDR2/HPH2 (Edr2/Mph2/Phc2). Bmi1-deficient mice are characterized by progressive

*Corresponding author. Institute of Biochemistry, Hannover Medical School, Carl-Neuberg-Str.1, 30625 Hannover, Germany.
Tel.: +49 511 532 2825; Fax: +49 511 532 2827;
E-mail: gaestel.matthias@mh-hannover.de
[4]These authors contributed equally to this work
[5]Present address: Department of Immunobiology, Yale University School of Medicine, New Haven, CT 06520, USA

Received: 10 October 2008; accepted: 24 March 2009

loss of HSCs and cerebellar neurons (van der Lugt *et al*, 1994). More recently, direct evidence implicated Bmi1 in the self-renewal of stem cells (Lessard and Sauvageau, 2003; Molofsky *et al*, 2003; Park *et al*, 2003). Similarly, Mph1/Rae28-deficient HSCs show decreased proliferative and self-renewal capacity (Ohta *et al*, 2002; Park *et al*, 2003). In addition to defects in the homeostasis of HSCs, PRC1 and PRC2 PcG mutant mice also suffer from lymphoid differentiation defects (reviewed in Valk-Lingbeek *et al*, 2004) and, in case of Phc2/Edr2, from changes in skeleton and premature senescence (Isono *et al*, 2005). Thus, PcG proteins play a crucial role in regulating stem cell self-renewal and differentiation (recently reviewed in Rajasekhar and Begemann, 2007).

In vitro evidence indicates that MK2 and MK3 may selectively interact with EDR2/HPH2 and target components of PRC1 (Yannoni *et al*, 2004; Voncken *et al*, 2005), suggesting a functional link between MAPKAP kinases and polycomb proteins. Here, we analyse the interaction between mouse PRC1 and MK2 and unequivocally document a role for the MK2 complex in maintaining the 'stemness' of HSCs *in vivo*.

Results

Phenotypic characterization of haematopoietic stem cells of MK2−/− mice

To numerically assess HSCs, we first quantified the Lin-(CD3ε−, CD11b−, B220−, Gr-1−, TER119−)-Sca1 + c-Kit + (LSK) population, classically defined as the HSC compartment. Compared with wild-type mice cells, LSK cells appeared to have increased in relative and absolute numbers in MK2−/− mice (Figure 1A and B). As LSK cells contain LT-HSC, ST-HSC, ELPs and multipotent progenitors, we also analysed HSCs defined by expression of SLAM family receptors (Kiel *et al*, 2005). As shown in Figure 1B and C, MK2−/− mice showed a decrease in CD150 + CD48− cells compared with wild-type control mice. Furthermore, upon staining total bone marrow with the Hoechst dye 33342, MK2−/− mice showed a five-fold reduction in side population (SP) cells, known to contain quiescent HSC (Goodell *et al*, 1996) (Figure 1D). LSK cells were further analysed for expression of CD34 and Flt3 to differentiate long-term (LT) (CD34−Flt3−)-, short-term (ST) (CD34 + Flt3−)-HSCs and multipotent progenitor cells (MPPs)(CD34 + Flt3 +). The relative proportion and absolute number of LT-HSCs are decreased in MK2−/− mice whereas these values are increased for MPPs (Figure 1E and F). To assess whether the lack of MK2 has any effects on the differentiation of HSC, we analysed erythroid, myeloid, and lymphoid cells in the bone marrow and spleen. In consistence with the results published earlier (Kotlyarov *et al*, 1999), the proportions of TER119, CD11b and Gr1 were not different between MK2−/− and control mice; furthermore, no differences were seen in phenotypic studies characterizing common lymphoid and myeloid progenitor cells (Supplementary Figures 1–5). In addition, by blood cell count we could not detect a haematopoietic failure in 4-, 8- and 12-months old mice, thus confirming data published earlier (Hegen *et al*, 2006; Jagavelu *et al*, 2007). These findings indicate that the HSC pool is significantly reduced in MK2−/− mice, whereas differentiation of HSCs and progenitor cells is not affected.

Functional characterization of MK2-deficient HSC

We hypothesized that inefficient PcG-mediated transcriptional repression may lead to a release of the actively maintained state of quiescence in HSC. This, in turn, should be associated with increased proliferative responses of HSCs to cytokines. To directly measure the HSC proliferation, we isolated LSK cells from wild-type and MK2−/− mice and cultured them in the presence of a recombinant cytokine cocktail consisting of SCF, IL3, IL6, Flt3L and TPO. As expected, MK2−/− LSK cells showed a significantly higher proliferative response as assessed by ^{3}H-thymidine incorporation (Figure 2A). We were also interested in monitoring the proliferation of different HSC sub-populations in the absence of cytokine stress *in vivo*. MK2−/− and wild-type mice were fed with BrdU for 48 h, and the BrdU incorporation into LSK cells was determined by FACS analysis. MK2−/− LT-, ST-HSCs and MPPs showed increased staining for BrdU (Figure 2B), indicating that enhanced proliferation of HSC is not only associated with cytokine exposure *in vitro* but also occurs in the physiological bone marrow environment *in vivo*.

To further assess a putative state of promoted cell-cycle progression in LSK cells, we carried out cell-cycle analysis using propidium iodide staining of *in vitro*-cultured LSK cells as well as LSK cells directly prepared from mice. In comparison with wild-type cells, MK2−/− cells showed fewer cells in G1/G0 phase and more cells in S and G2/M phases (Figure 2C), thus confirming increased cell-cycle progression in the absence of MK2. Cyclin-dependent kinase inhibitors are important mediators of cell quiescence and serve as checkpoints, restricting cell-cycle transition. P21Cip1Waf1-deficient HSCs show impaired self-renewal and increased proliferation (Cheng *et al*, 2000). To determine the expression levels of P21Cip1Waf1, we carried out RT–PCR analysis in CD150 + CD48− HSCs from MK2−/− and wild-type mice. As shown in Figure 2D, MK2−/− CD150 + CD48− HSCs show decreased abundance of p21Cip1/Waf1 mRNA, a finding in line with accelerated cell cycle progression in MK2−/− cells. Similar findings of decreased p21 mRNA level and increased cell-cycle progression were reported in Gfi1-deficient HSCs (Hock *et al*, 2004). To shed light on the molecular mechanism of reduced stem-cell quiescence, we determined expression levels of direct downstream targets of Bmi1, p16Ink4a and p19Arf. In the absence of Bmi1, repression of the Ink4a locus is relieved, resulting in expression of p16Ink4a and p19Arf (Jacobs *et al*, 1999). As shown in Figure 2E, MK2-deficient CD150 + CD48− HSCs show higher expression levels of p19Arf, whereas the expression levels of Ink4a and p27 (Kip1) were comparable to those of wildtype control cells (data not shown).

Cytokine-induced proliferation of HSC *in vitro* is associated with loss of 'stemness'. We hypothesized that the sequence of events resulting in loss of stemness might occur more rapidly in unrestricted proliferation of MK2-deficient HSC. As no phenotypic marker unequivocally reflects HSC function, we monitored the cell-surface expression of Sca1 as a surrogate parameter for early haematopoietic progenitor activity. CD150 + /CD48− HSCs from MK2−/− and wild-type mice were sorted (Figure 3A, upper panel) and cultured *in vitro* in the presence of the recombinant cytokines SCF, IL3, IL6, Flt3L, and TPO. Immediately after cell sorting, both MK2−/− and wild-type CD150 + /CD48− HSCs showed an

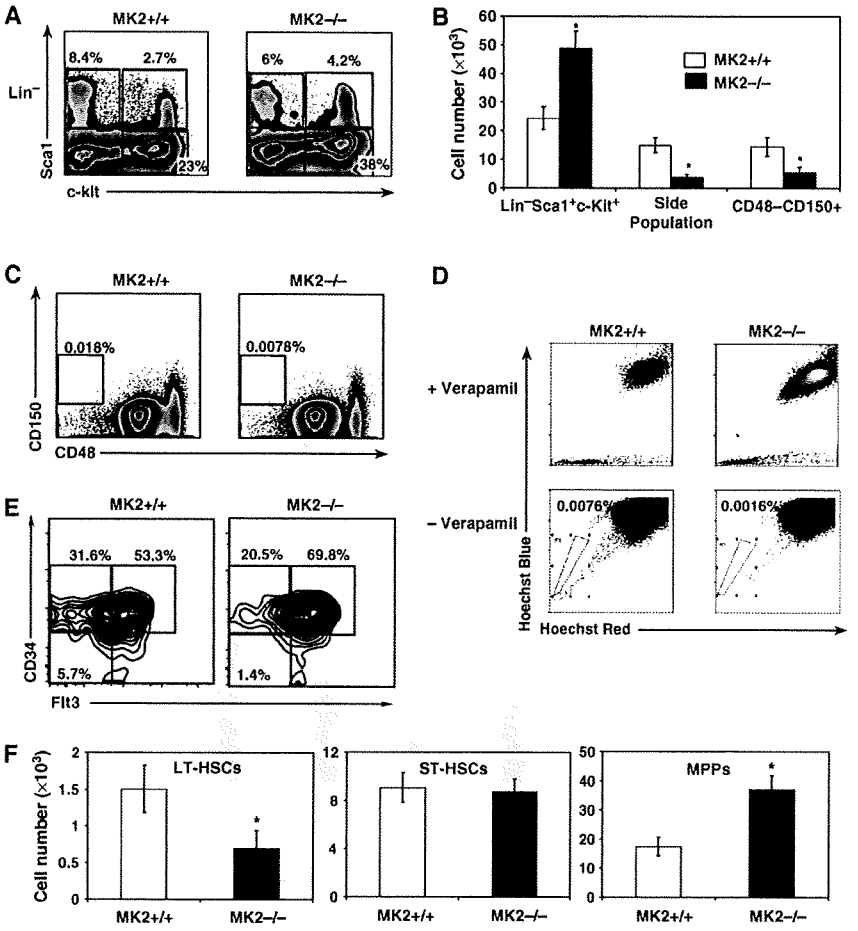

Figure 1 Phenotypic analysis of the haematopoietic stem cell compartment in MK2−/− mice. (**A**) FACS plots indicating relative increase of LSK cells in MK2−/− mice. Lineage-marker (CD3ε, CD11b, B220, Gr-1, TER119)-negative cells were gated and further analysed for expression of Sca1 and c-Kit. Data are representative of three independent experiments. (**B**) Absolute numbers of LSK, SP and CD150+ CD48− cells determined from the bone marrow of both hind limbs ($N=6$ mice). Data are representative of two independent experiments. Asterisks indicate statistical significance ($P<0.01$). (**C**) FACS plots indicating reduced frequency of CD150+ CD48− cells in MK2−/− mice. Data are representative of two independent experiments. (**D**) Side population (SP) analysis upon staining of BM cells with Hoechst 33342 dye. Cells stained with Hoechst 33342 dye in the presence of verapamil serve as controls for the specificity of the SP population. Data are representative of two independent experiments. (**E**) FACS plots indicating relative decrease of long-term (LT)-HSCs (CD34−Flt3−LSK) and short-term (ST)-HSCs (CD34+Flt3−LSK), and increase of multipotent progenitor cells (MPPs) (CD34+Flt3+LSK) in MK2−/− mice. Total BM cells of MK2+/+ and MK2−/− were prepared and stained with an antibody cocktail that recognizes lineage markers (CD11b, Gr1, B220, CD3e, TER119), Sca1 and c-Kit, and analysed by flow cytometry. LSK cells were pre-gated and further analysed for CD34 and Flt3 expression. (**F**) Absolute numbers of LT-HSCs (left), ST-HSCs (middle) and MPPs (right) determined from the bone marrow of both hind limbs ($N=5$ mice). Asterisks indicate statistical significance ($P<0.05$). Data in (E) and (F) are representative of three independent experiments.

equal pattern of expression of c-Kit and Sca1 (Figure 3A, middle panel). However, after 3 days *in vitro*, only between 16–21% of MK2−/− progenitor cells stained positive for Sca1, whereas between 60–75% of wild-type progenitor cells maintained Sca1 expression (Figure 3A, lower panel and quantification below), suggesting that MK2 is crucial for the maintenance of an early state of differentiation or quiescence. Similar results were obtained for LSK cells (data not shown). To assess whether cytokine-stimulated HSCs showed a skewed differentiation, we analysed the expression of lineage-specific cell surface markers. In comparison to wildtype cells, a larger fraction of MK2-deficient cells showed expression of CD11b and Gr1 (Supplementary Figures 6 and 7). Analysis of CD150+/CD48− HSCs using a CFSE dilution assay indicates higher proliferation of MK2-deficient cells (Figure 3B) similar to LSK cells (Figure 2A–C).

The *in vitro* culture system described above allowed us to test whether a direct inhibitor of p38 MAPK signalling similarly unleashes HSC quiescence. Wild-type LSK cells were purified and incubated for 48 h in the absence or presence of 5 μM SB239063, which does not reduce the overall viability of the cells (Supplementary Figure 8). As shown in Figure 3C, cells exposed to a specific p38 inhibitor almost completely lost the expression of Sca1, whereas cells stimulated in the absence of SB239063 remained largely positive for expression of Sca1. These findings corroborate the idea that p38 signalling is crucial for the maintenance of HSC quiescence.

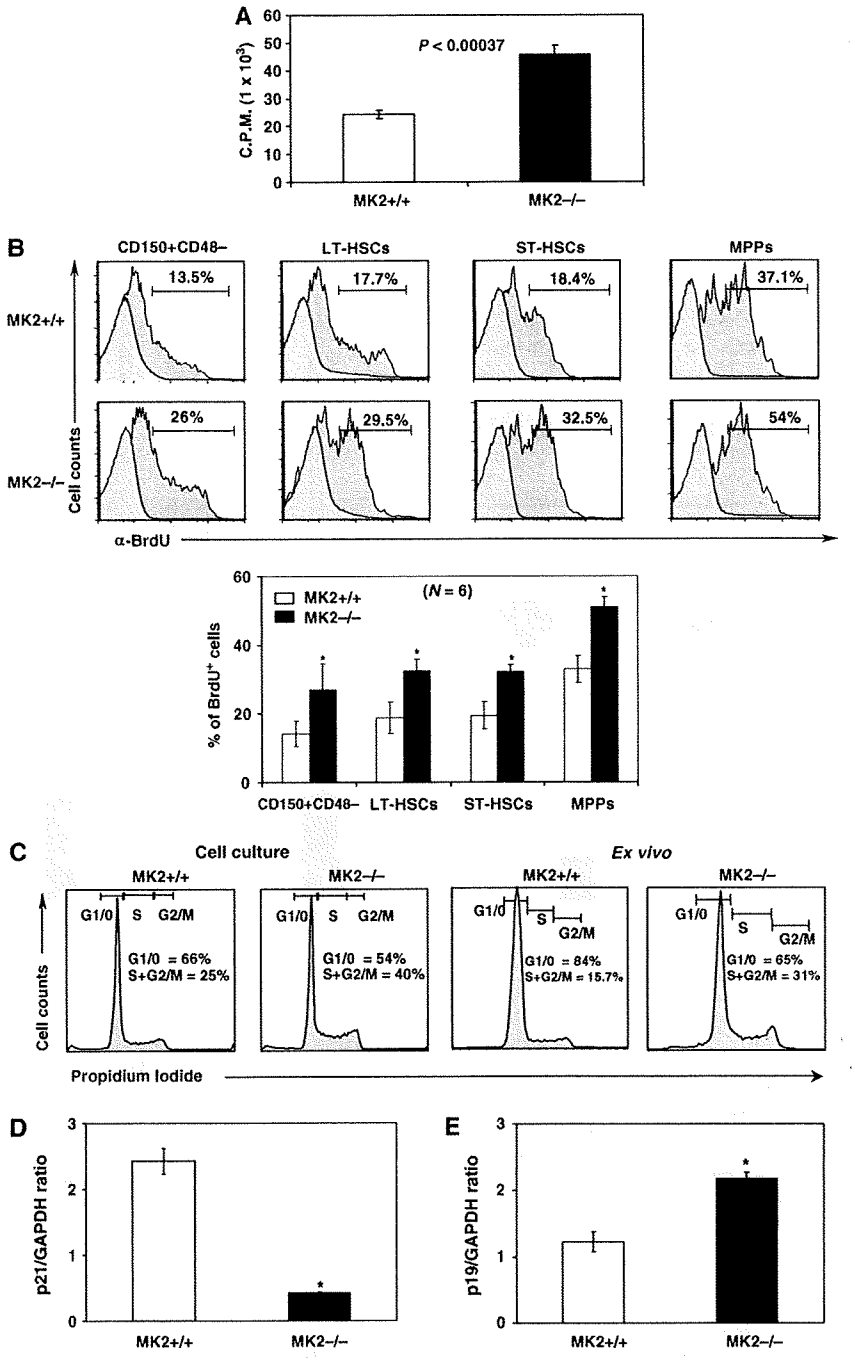

Figure 2 Increased proliferation of LSK in MK2−/− mice. (**A**) *In vitro* proliferation assay. Purified LSK cells were cultured in the presence of recombinant cytokines for 48 h, pulsed with ^{3}H-thymidine, and subjected to scintillation counting. The mean values of triplicate samples are shown. (**B**) *In vivo* BrdU incorporation experiment. The *in vivo*-proliferation potential of CD150 + CD48− cells, LT-HSCs, ST-HSCs and MPPs in MK2 + / + and MK2−/− mice was measured after feeding BrdU through drinking water for 2 days. RBC-depleted BM cells were stained with monoclonal antibodies recognizing subsets of HSCs and BrdU (negative controls of cells from mice fed with PBS are shown as insets in light grey). Indicated HSC subsets were pre-gated and histograms were generated for quantifying the incorporated BrdU (% of BrdU-positive cells is given). Data are representative of two independent experiments. Cells from three mice from each of the two experiments were measured separately ($N = 6$). Mean and statistics are in the diagram given below (asterisks indicate significant differences with $P < 0.05$). (**C**) Cell-cycle analysis. Purified LSK cells were cultured *in vitro* in the presence of recombinant cytokines for 48 h. Cells were fixed, stained with propidium iodide and their DNA content was measured by flow cytometry (left panel). LSK cells isolated from MK2 + / + and MK2−/− mice were sorted, directly fixed and stained with propidium iodide, and their DNA content was measured by flow cytometry (right panel). (**D**, **E**) Real-time PCR showing p21Cip1/Waf1 (D) and p19Arf mRNA levels (E) in purified CD150 + CD48−HSCs. The mean values of duplicate samples are shown. Asterisks indicate statistical significance ($P < 0.01$). Data are representative of two independent experiments each.

To directly assess the self-renewal capacity of HSC, we carried out competitive repopulation experiments. Various numbers of wild-type and MK2−/− bone marrow cells (CD45.2) were mixed with 10^5 wild-type CD45.1 competitor cells and transplanted into lethally irradiated CD45.1 recipient mice. Three months later, the mice were killed and the specific contribution of CD45.1 and CD45.2 cells to haematopoiesis was assessed by FACS analysis. In line with earlier experiments (Kotlyarov *et al*, 1999) and the data shown in Supplementary Figures 1–5, no defect of differentiation in various haematopoietic lineages could be observed in mice transplanted with MK2−/− cells (data not shown), confirming that MK2 is not crucially involved in controlling HSC differentiation. When 10^5 HSCs were mixed with 10^5 competitor cells, MK2-deficient cells contributed to 54% of haematopoiesis, whereas wild-type cells contributed to 75% of haematopoiesis. However, under limiting conditions, when fewer HSCs were transplanted, the statistically significant

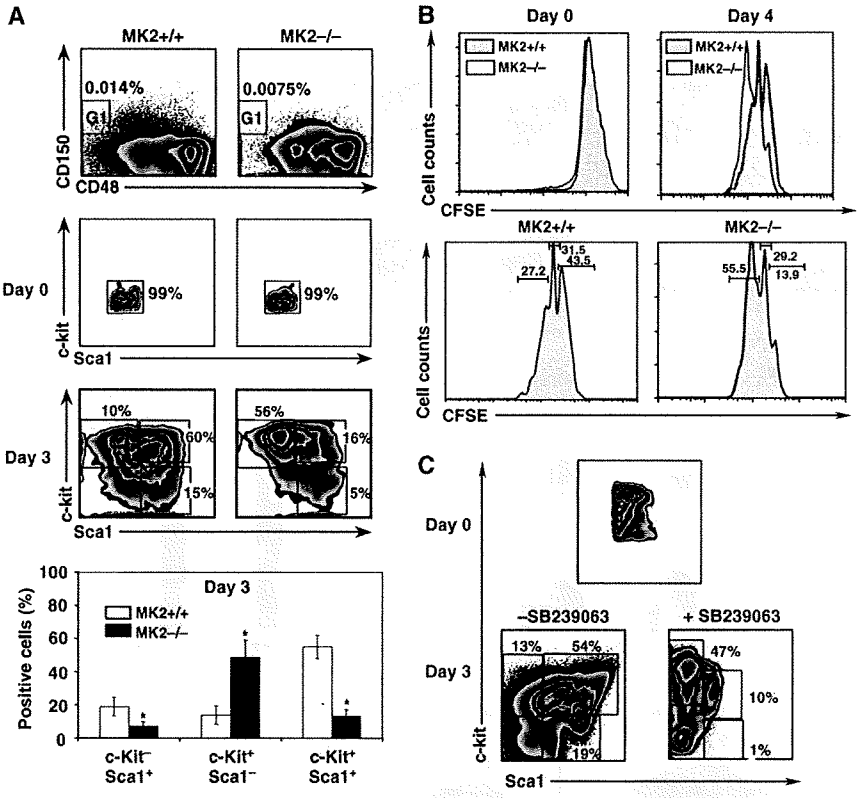

Figure 3 Compromised haematopoietic stem cell function in MK2−/− mice. **(A)** Contour plots indicating an accelerated loss of Sca1 expression in MK2−/− SLAM cells *in vitro*. The upper panel shows sorting of SLAM cells, the middle panel shows expression pattern of Sca1 and c-Kit in primary sorted SLAM cells; and the two lower panels show Sca1 and c-Kit expression after 3 days of *in vitro* culture in the presence of recombinant cytokines. Cell subsets were discriminated on the basis of differential expression of Sca1 and c-Kit, their percentages were calculated and plotted. Asterisks indicate statistical significance ($P<0.01$). Data are representative of two independent experiments. **(B)** CFSE-proliferation assay for WT and MK2-deficient SLAM cells. Sorted CD150+CD48− HSCs of MK2+/+ and MK2−/− mice were stained with CFSE and cultured *in vitro* in the presence of cytokine cocktail for 3 days. On day 4, aliquots of cells were analysed by flow cytometry. Histograms, documenting increased *in vitro* proliferation of MK2−/− CD150+CD48− HSCs, as assessed by the percentage of cells that appear under gates that measure each cycle of proliferation. **(C)** FACS plots indicating an accelerated loss of Sca1 expression in MK2+/+ cells in the presence of the MAPK p38 inhibitor SB239063. The upper panel shows the expression pattern of Sca1 and c-Kit in primary sorted LSK cells, lower panels show Sca1 and c-Kit expression after 3 days *in vitro* culture containing recombinant cytokines in the presence or absence of SB239063, respectively. Data are representative of two independent experiments. **(D)** Competitive repopulation experiment. 10^5 CD45.1$^+$ competitor BM cells were mixed with defined numbers of CD45.2+ MK2+/+ or CD45.2+ MK2−/− BM cells, and total BM was analysed for competitive repopulation as described. A characteristic experiment (left) and statistical evaluation (right) ($N=5$) are shown. Asterisks indicate statistically significant ($P<0.05$, single sided *t*-test) differences between MK2-deficient and wildtype cells. **(E)** Competitive repopulation assay as in (D), but using 10^4 CD45.1+ competitor LSK cells mixed with defined numbers of CD45.2+ MK2+/+ or CD45.2+ MK2−/− LSK cells in lethally irradiated (9.5 Gy) CD45.1+ congenic recipients. A characteristic experiment (left) and statistical evaluation (right) ($N=10$) are shown. Asterisks indicate statistically significant ($P<0.05$, single-sided *t*-test) differences between MK2-deficient and wildtype cells. **(F)** Secondary transplantation of 2×10^6 WT and MK2−/− bone marrow cells (CD45.2) mixed with 10^5 competitor cells. Analysis was performed 16 weeks after transplant. A characteristic experiment (left) and statistical evaluation (right) ($N=5$) are shown. Asterisks indicate statistically significant ($P<0.05$, single-sided *t*-test) differences between MK2-deficient and wildtype cells. **(G)** FACS plots and quantification indicating reduced frequencies of CD150+CD48− HSCs in CD45.1 WT congenic recipients that received MK2−/− LSK cells. Sorted LSK (CD45.2) cells of MK2+/+ and MK2−/− mice were transplanted into lethally irradiated CD45.1 wildtype recipients. At 16 weeks after transplantation, donor-derived (CD45.2) haematopoietic cells of BM were pre-gated and analysed for CD150 and CD48 expression (left). Absolute numbers of donor (CD45.2)-derived CD150+ CD48− cells were determined from the bone marrow of both hind limbs ($N=5$ mice). The asterisk indicates statistically significance ($P<0.05$). Data are representative of two independent experiments.

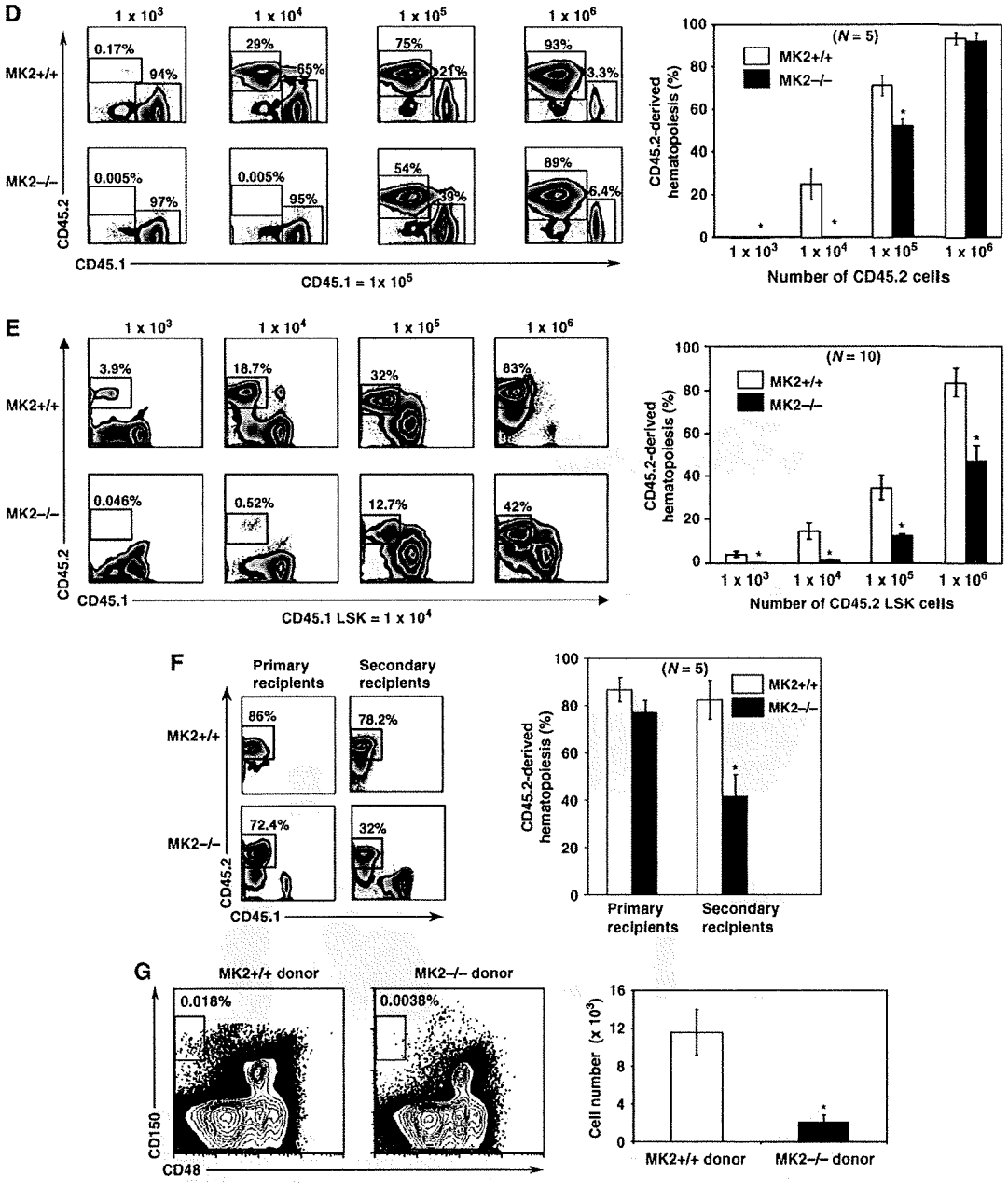

Figure 3 Continued.

difference between MK2-deficient cells and wildtype cells was striking (0.005 versus 29% for 10^4 HSCs and 0.005 versus 0.17% for 10^3 HSCs) (Figure 3D). Hence, MK2−/− HSCs showed an obvious disadvantage in their repopulation capacity, when compared with wild-type cells. To confirm and to further extend this finding, the repopulation experiment was also carried out with the LSK cell fraction enriched in HSCs. A similar defect was observed with respect to the LSK-repopulation capacity of MK2−/− cells (Figure 3E). We also carried out a secondary transplant experiment to confirm the self-renewal capacity of HSCs. Mice transplanted with a cell population of 2×10^6 WT and MK2−/− bone marrow cells (CD45.2) mixed with 10^5 competitor cells showed a mild reduction of CD45.2-positive MK2−/− cells compared with WT cells 12 weeks after transplantation (Figure 3F, primary recipients). When 2×10^6 bone marrow cells of these primary recipients were transplanted into secondary recipients, a defect of MK2−/− HSC became manifest (32% CD45.2 MK2−/− cells versus 78% CD45.2 MK2+/+ cells) (Figure 3F, secondary recipients), almost independently of addition of wild-type competitor cells (Supplementary Figure 9). Finally, the restoration of the CD150+CD48− HSC compartment after transplantation into WT mice, depending on the genotype of the donor cells, was analysed and was shown to be reduced for MK2-deficient donor cells (Figure 3G). Together these experiments show that a decreased quiescent

HSC pool in MK2−/− mice results in functional impairment under stress conditions.

Identification of Edr1 and Edr2 as interaction partners of MK2

To identify new interacting proteins for mouse MK2, a yeast-two-hybrid screen was carried out using a murine day-11-embryo brain library. The analysis revealed 27 positive clones: three of them carried cDNAs of the known MK2-interaction partner p38α, 17 clones carried 11 different cDNA fragments coding for C-terminal parts of mouse Edr1 ($n=4$), p36-Edr2 ($n=6$) and p90-Edr2 (Yamaki *et al*, 2002) ($n=1$). Interestingly, all Edr1/2 clones contained a single zinc-finger domain with the FCS signature followed by the region coding for the C-terminal homology domains (HD) II and III. HDII is also known as a sterile alpha motif (SAM) domain that has been shown to self-associate, bind to other SAM domains or form heteromeric interactions with some non-SAM domains of other proteins (Qiao and Bowie, 2005). The specificity of MK2–Edr1/2 interaction was confirmed by GST-pull-down experiments upon recombinant expression in *Escherichia coli*, using His-p38α/GST-MK2 interaction as a positive control. As shown in Figure 4A, His-Edr1 and His-Edr2 specifically bind to GST-MK2 but not to GST. In subsequent experiments, we limited our investigations to Edr2 interactions, as ectopic overexpression of Edr1 in mammalian cells was inefficient and available antibodies showed a low degree of specificity. Specific interaction of MK2 with endogenous Edr2 was shown by GST pull-down of endogenous Edr2 from HEK293-T cells transfected with different GST constructs (Figure 4B). Although endogenous Edr2 was found to bind to GST-MK2 and to the GST fusion of the structurally closely related MK3, which is expressed in LSK cells at levels comparable to MK2 (Supplementary Figure 10), as well as to the PcG member GST-Bmi1—used here as a positive control, GST fusion of the structurally more distant MK5, GST-MK5, was not able to bind Edr2 efficiently. We then extended the analysis of MK2–Edr2 interaction by carrying out co-immunoprecipitation of endogenous MK2 and Edr2 from mouse embryonic fibroblasts (Figure 4C). The specificity of the positive signal is shown by inefficient co-immunoprecipitation from lysates of MK2/3-deficient fibroblasts.

MK2 interacts with PRC1

Next, we were interested to know whether MK2 interacts with Edr2 within the physiological PRC1 complex. To this end, we tried to detect another core component of PRC1, the ring finger protein Ring1B, in the protein fraction bound to GST-MK2. As a negative control, we used again a GST-MK5 pull-down. As shown in Figure 4D, MK2, but not MK5, precipitates Ring1B, supporting the notion that MK2 is able to interact with the physiological PRC1 complex. To rule out the possibility that this interaction is because of the ectopic overexpression of the recombinant fusion proteins, we analysed the co-existence of the endogenous proteins in high molecular-weight fractions from lysates of mouse embryonic fibroblasts (MEFs). Lysates were separated by gel filtration and protein fractions were analysed by western blot using antibodies against Ring1B and MK2 (Figure 4E). In lysates from wildtype MEFs, co-separation of Ring1B and a small sub-population of MK2 can be detected in a fraction corresponding to a molecular mass of about 1MDa (asterisk). To show the specificity of the bands for MK2, we repeated this analysis with lysate from MK2-deficient MEFs. Although Ring1B can be detected in the corresponding fraction, the two corresponding bands for MK2 (boxed) are missing. This supports the notion that a sub-population of endogenous MK2 exists in the 1-MDa fraction, reflecting its interaction with endogenous PRC1. This interaction obviously does not include p38 MAPK, as it cannot be detected in the 1-MDa fraction (data not shown).

Edr2 and MK2 co-localize in polycomb bodies characteristic for PRC1

MK2 and p38α exist as a complex in the nucleus of resting cells. Upon activation of the p38 MAPK cascade, MK2 is phosphorylated, activated, and because of de-masking of a nuclear export signal, translocates to the cytoplasm (Ben-Levy *et al*, 1998; Engel *et al*, 1998; Neininger *et al*, 2001). In view of this finding, we hypothesized that a physiologically relevant nuclear PRC1–MK2 interaction may be released upon activation of the p38 MAPK cascade. First, we analysed the sub-cellular localization of MK2 and Edr2 in quiescent HEK293 cells upon transfection with MK2–YFP and Edr2–CFP fusion constructs. Both proteins showed perfect co-localization in speckles in the nucleus (polycomb bodies), reminiscent of the characteristic distribution pattern of proteins organized in PRC1 complexes such as endogenous Edr1, Edr2, Bmi1 and Ring1B (Suzuki *et al*, 2002) (Figure 5A). Second, we visualized stress-dependent translocation of GFP-MK2 in HeLa cells co-transfected with HA-Edr2. In contrast to our hypothesis, arsenite-induced stress activation of the p38 MAPK cascade did not trigger complete translocation of MK2 into the cytoplasm. In strict dependence on Edr2 co-expression, a sub-fraction of MK2 was retained in the polycomb bodies (Figure 5B), suggesting that activated MK2 alone or in complex with p38 may also have a physiological function at the nuclear PRC1 (cf. also schematic presentation of Figure 7).

Identification of the Edr2-interacting region in MK2

To further dissect the molecular interaction between MK2 and Edr2, we carried out GST–Edr2 pull-down assays using GFP fusion proteins with defined MK2 subdomains. Two regions of the small lobe of the kinase, subdomains I–III (amino acids 29–99) and IV-V (amino acids 97–131), are sufficient to interact with Edr2 (Figure 6A and B), indicating that both regions contribute to the interaction. The specific role of these subdomains for interacting with Edr2 was further substantiated using a MK2/MK5 hybrid molecule. When amino acids 38–128 are replaced by the homologous region of MK5, the hybrid molecule no longer binds to Edr2, as shown in pull-down experiments (Figure 6C), as well as in the co-localization assay (Figure 6D). As these domains do not overlap with the C-terminal docking site for p38α at amino acids 371–375 (Tanoue *et al*, 2000), it is possible that MK2, Edr2 and p38 can form a ternary complex at PRC1.

Functional rescue of MK2-deficient HSCs requires Edr2-binding of MK2

Finally, we were interested to determine a direct functional link between the HSC phenotype of MK2−/− mice and the Edr2-binding properties of MK2. To address this issue, we made use of the MK2/5 hybrid molecule, which is unable to

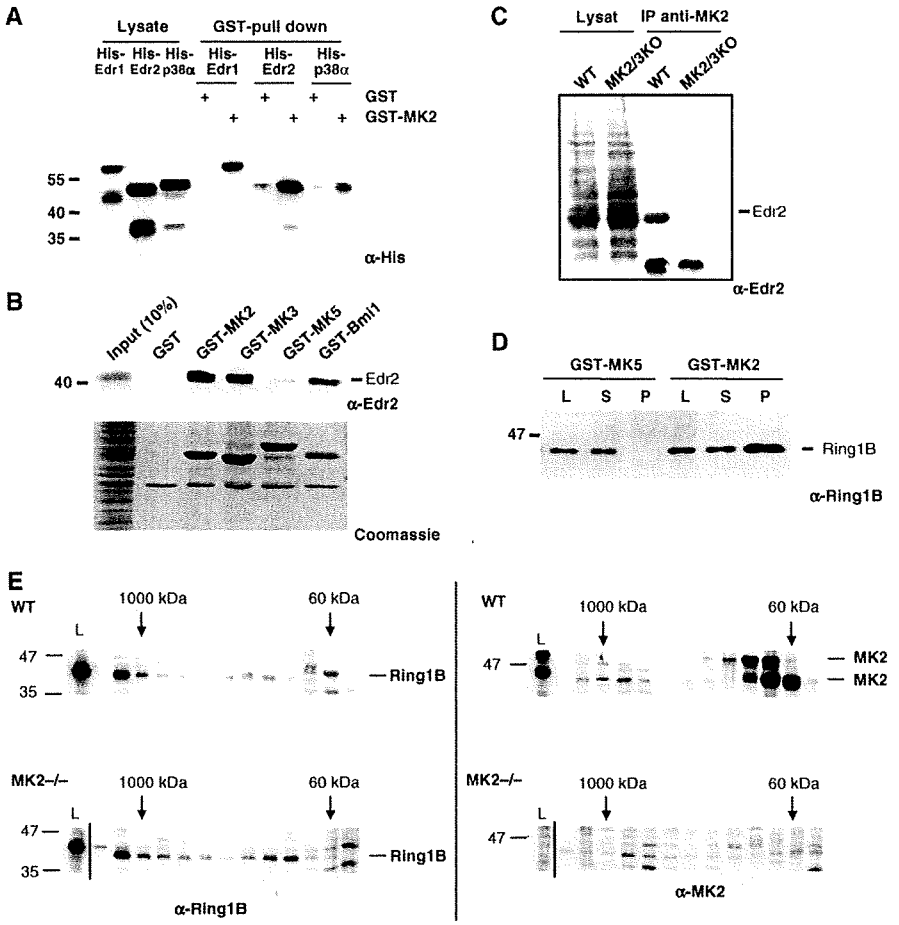

Figure 4 Interaction of MK2 with PRC1 components. (**A**) MK2 interaction with recombinant Edr1 and Edr2 *in vitro*. GST pull-down (right) of recombinant 6-His-tagged Edr1/2 from *E. coli* lysate. As a positive control, 6-His-tagged p38α is used; as negative control pull-down is performed with GST alone. Total *E. coli* lysates are separated at the left. His-tagged proteins are detected by anti-hexahistidine western blot. (**B**) Interaction of MK2 with endogenous Edr2. Whole-cell lysate of transfected HEK 293-T cells were used in a GST pull-down with recombinant GST-MK2, GST-MK3, GST-MK5, GST (negative control) and GST-Bmi1 (positive control). Comparable expression and GST pull down of the fusion proteins was monitored by Coomassie protein staining. Specific interactions of GST-MK2, GST-MK3 and GST-Bmi1 with endogenous Edr2 were detected by western blot using Edr2 antibodies. (**C**) Co-IP of endogenous MK2 and Edr2 from WT mouse embryonic fibroblasts (MEFs) but not from MK2/3-deficient (MK2/3 KO) MEFs (negative control). (**D, E**) MK2 interaction with the PRC1 complex. (D) Lysates (L) from HEK 293 cells overexpressing Edr2 were subjected to GST pull-down using GST-MK2 and, as negative control, GST-MK5. Supernatant (S) and pull-down (P) were analysed for PRC1 complexes by western blot against the PRC1 component Ring1B. (E) Co-separation of endogenous Ring1B and endogenous MK2 in a high-molecular-weight fraction. Nuclear extracts from wildtype (WT) and MK2-deficient MEFs (MK2−/−) were applied to FPLC gel filtration using a Superose 6 HR 10/30 column. Proteins from load (L) and fractions were subsequently separated by SDS–PAGE. In both lower panels, an empty lane between load and fractions was cut out from the blot to align corresponding molecular-weight fractions between the analysis of WT (upper panel) and MK2-deficient (lower panel) cells. Ring1B and MK2 were detected by western blot. The approximate size of the native proteins in the chromatographic fractions is indicated on the top. The protein size in SDS–PAGE is indicated left. The Ring1B band and the two MK2-specific bands are indicated at the right of each blot. The bands representing the sub-population of MK2 in the high-molecular-weight fraction are marked by a box with asterisk in the anti-MK2 blot of separation of WT lysate. The corresponding region of separation of MK2-deficient lysate lacking these bands is also boxed. The MK2 antibody decorates also several bands in the lysate of MK2-deficient cells (MK2−/−) probably because of cross-reaction with MK3 and because of non-specific binding.

associate with Edr2 (see Figure 6C and D) but maintains full catalytic kinase activity, as shown in MK2/3 double knockout cells (Figure 6E). MK2/3 double-knockout embryonic fibroblasts do not display any stress-induced Hsp25 phosphorylation. In contrast, retrovirus-mediated expression of MK2/5 and MK2 yielded a comparable level of Hsp25 phosphorylation upon UV stimulation. Hence, MK2 and MK2/5 are indistinguishable with respect to their kinase activity and differ only in Edr2 binding, allowing the dissection of kinase function from Edr2-mediated effects in the MK2/5 hybrid kinase. We hypothesized that MK2-deficient cells would be reconstituted by MK2 but not by the MK2/5 hybrid kinase with respect to stem-cell fitness.

The viral constructs were then used to introduce MK2 and MK2/5 into lineage-marker negative MK2-deficient CD45.2 cells, yielding similar transduction rates (30%) as assessed by expression of the marker gene GFP. 10^4 bi-cistronic expression construct-transduced CD45.2 MK2-deficient LSK cells were mixed with the same number of control GFP-construct-transduced CD45.1 LSK WT competitor cells, transplanted into lethally irradiated CD45.1 recipient mice, which were analysed 3 month later. As seen in Figure 6F,

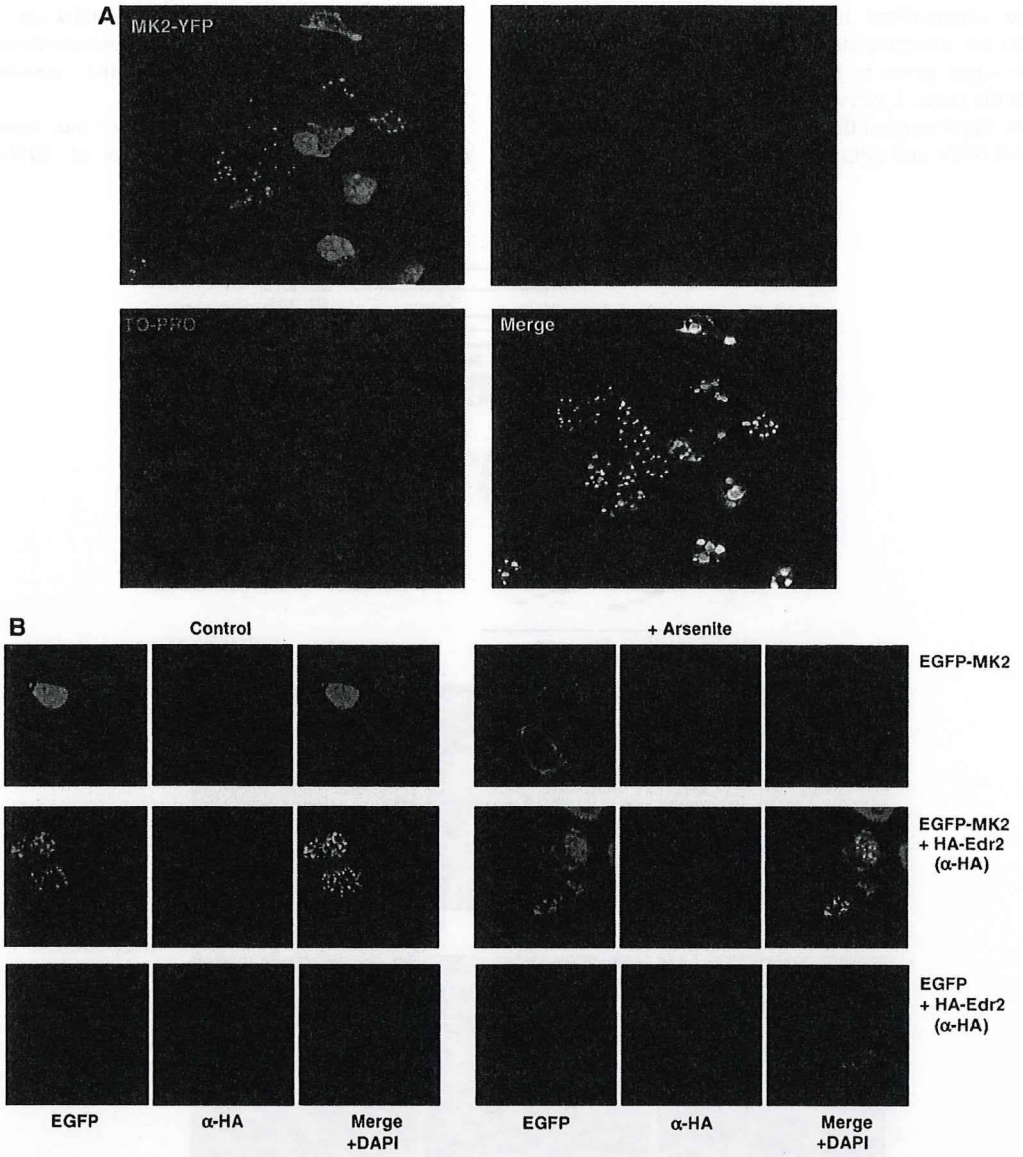

Figure 5 Co-localisation of MK2 and Edr2 in polycomb bodies characteristic for PRC1. (**A**) HEK 293 cells were transfected with constructs coding for an MK2-yellow fluorescent protein (YFP) fusion and an Edr2-CyAn fluorescent protein (CFP) fusion. Fusion proteins were visualized by fluorescence microscopy. Nuclei were stained using TO-PRO. (**B**) Stress-dependent changes in subcellular localizations of a GFP–MK2 fusion protein (GFP-MK2) in HeLa cells in the absence and presence of HA-tagged Edr2 (HA-Edr2). In the absence of HA-Edr2, arsenite treatment (+Arsenite) leads to export of evenly distributed GFP-MK2 from the nucleus. In cells overexpressing HA-Edr2 (+HA-Edr2), GFP–MK2 accumulates in polycomb bodies already before stress treatment (−Ars). Upon stress and in the presence of HA-Edr2, MK2 is translocated to the cytoplasm, but a sub-population of MK2 remains in polycomb bodies.

the LSK repopulation capacity of MK2−/− cells (6.8% in experiment 1 ($N=3$); 4.1% in experiment 2 ($N=3$)) is significantly increased by re-introduction of MK2 (42 and 49%), but not by the re-introduction of the Edr2 non-binding mutant of MK2, MK2/5 (0.4 and 0.2%). Taken together, this indicates that MK2–Edr2 interaction is essential for LSK repopulation capacity.

Discussion

MK2 is a downstream component of the p38 MAPK signalling cascade with pleiotropic functions. Acting as a protein kinase, MK2 controls the regulation of the actin cytoskeleton (Stokoe *et al*, 1992; Guay *et al*, 1997), stress-dependent small heat-shock protein phosphorylation (Vertii *et al*, 2006), and stability and translation of the AU-rich element containing cytokine mRNAs (Neininger *et al*, 2002; Hitti *et al*, 2006). Independently of its catalytic activity, MK2 stabilizes p38α (Kotlyarov *et al*, 2002) and could act as a shuttling protein, mediating nuclear export of p38α (Ben-Levy *et al*, 1998).

Here, we propose a new function for MK2 in maintaining HSC quiescence. This function involves MK2-targeting to PRC-1 through Edr1/2 binding and subsequent modulation of the transcriptional control mechanisms governing HSC

quiescence (summarized in Figure 7). This represents a mechanism for attracting signal-transducing protein kinases to specific target genes in mammalian cells as already described for the yeast, *S. cerevisiae* (Pokholok *et al*, 2006; Proft *et al*, 2006). We document the specific interaction of MK2 and members of PRC1 and define the regions involved in Edr2–MK2 interaction as a SAM domain on Edr2 and subdomains I–V in the small lobe of the kinase. The latter does not overlap with the p38α docking site on MK2, possibly allowing formation of a ternary complex.

Recently, the p38 MAPK pathway has been shown to control the lifespan of HSCs (Ito *et al*, 2006). Sustained

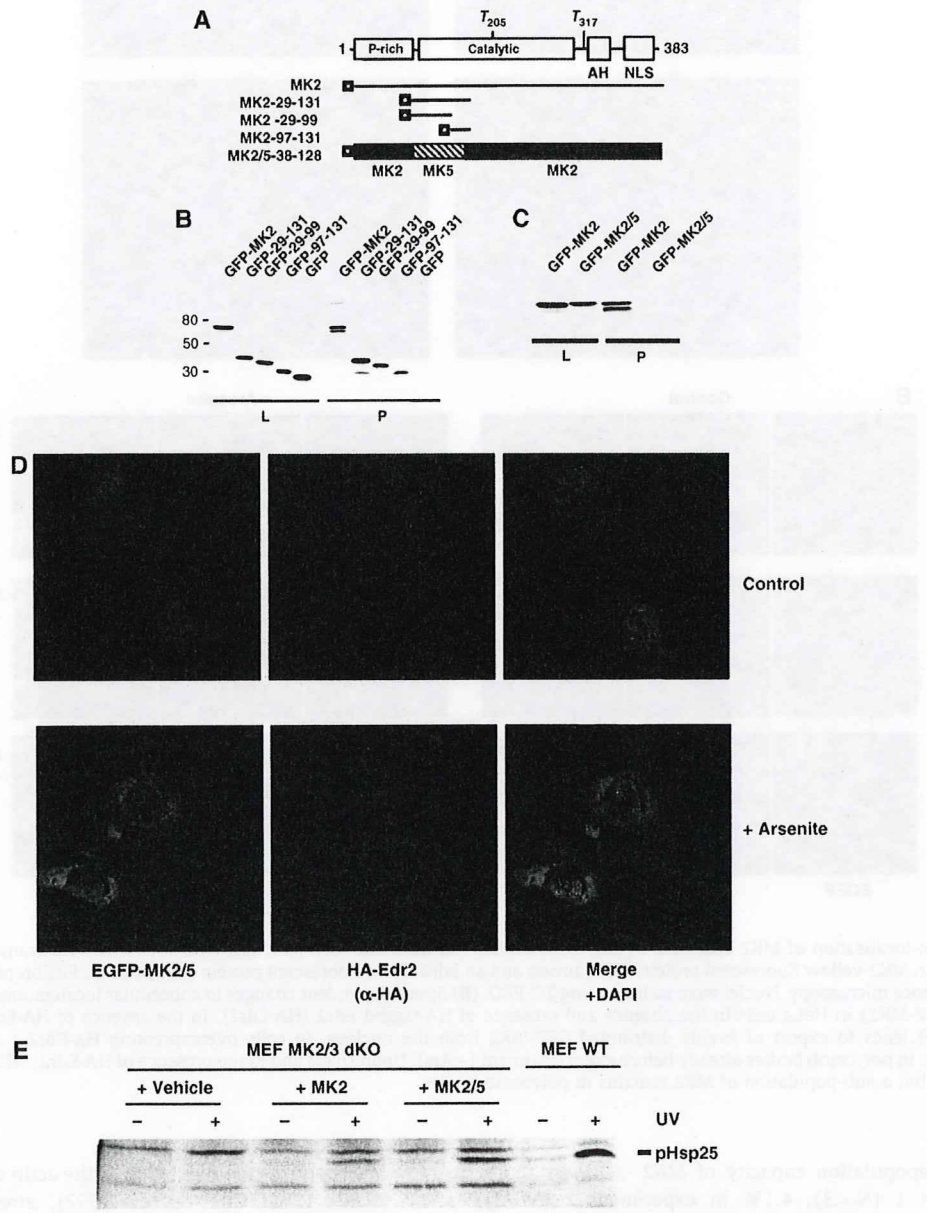

Figure 6 Identification of the Edr2-interacting region in MK2 and rescue of the repopulation capacity of MK2-deficient cells by MK2, but not by MK2/5. (**A**) Schematic representation of GFP–MK2, different GFP-tagged fragments of MK2, as well as an MK2/MK5 hybrid kinase (*P*-rich is the proline-rich N-terminal region, AH is the auto-inhibitory C-terminal helix containing the nuclear export signal (NES; Engel *et al*, 1998), NLS represents the nuclear localization signal and T205 and T317 are the regulatory phosphorylation sites of mouse MK2). (**B, C**) Lysates (*L*) from HEK 293 cells expressing the different GFP-tagged constructs described in (A) were subjected to GST-Edr2 pull-down (P). Proteins were detected by anti-GFP western blot. Molecular masses (kDa) are indicated in the left. (**D**) Comparable enzymatic activity of MK2 and MK2/5 against the *in vivo* substrate Hsp25 detected in transduced MEFs after UV stimulation (200 J/m^2) and 30 min recovery. (**E**) MK2/5 hybrid kinase misplaced from polycomb bodies (examined as in Figure 5B). (**F**) Competitive repopulation assay. 1×10^4 CD45.1 + LSK cells transduced with pMMP–IRES–GFP together with 1×10^4 CD45.2 + LSK cells transduced with the different bicistronic constructs indicated at the left were transplanted into recipient mice (CD45.1 +) and analysed for repopulation capacity as described. Two characteristic experiments and statistical evaluation (right) ($N = 6$) are shown. Asterisks indicate significant differences ($P < 0.01$) to vehicle-transduced cells. Transfection efficiency (about 30% for all three constructs) was monitored by GFP-expression.

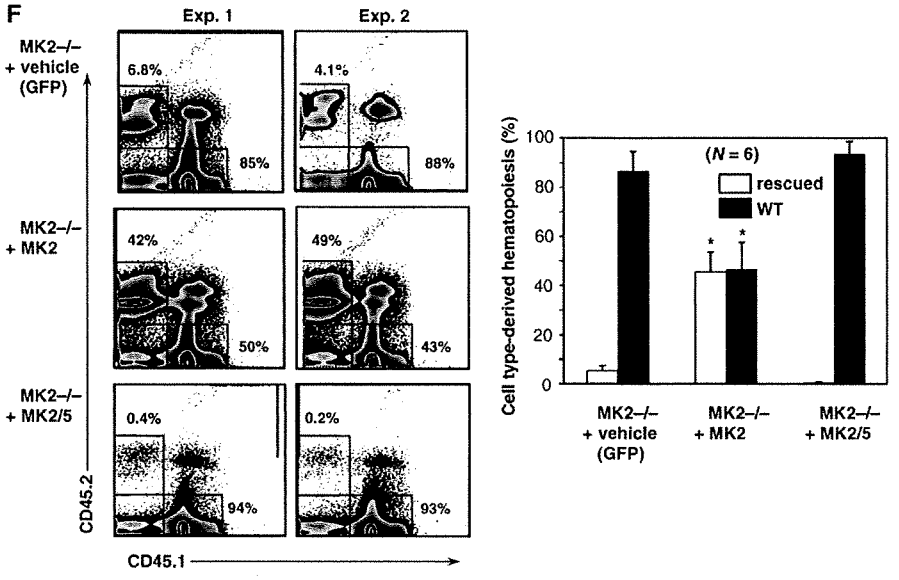

Figure 6 Continued.

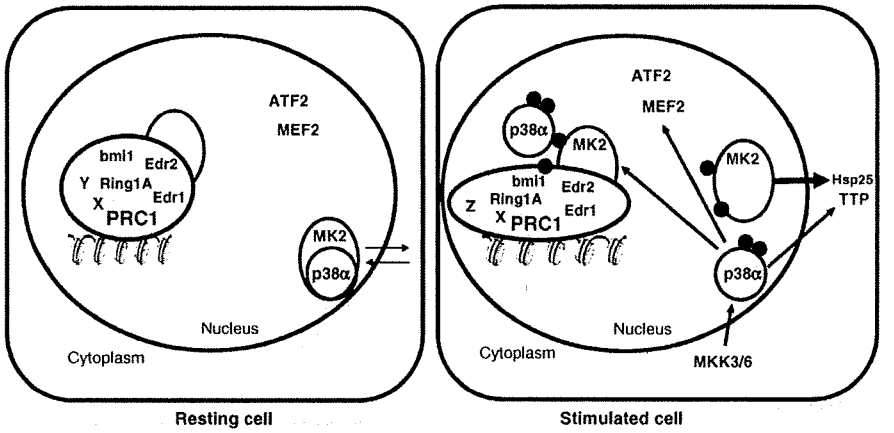

Figure 7 The model of stress -signalling to PRC1: In the nucleus of resting cells, a sub-population of MK2 (and MK3) is associated to PRC1 via specific interaction to Edr2 (and/or Edr1). A distinct, probably more abundant sub-population of MK2 (and MK3) exists in complex with p38α (or p38β). On stimulation of the p38 pathway, p38 is phosphorylated by MKK3 or MKK6 and, in turn, phosphorylates MK2 (and MK3). As a result of phosphorylation, the p38/MK2 complex becomes unstable (Lukas *et al*, 2004), the nuclear export signal of MK2 is unmasked (Neininger *et al*, 2001; White *et al*, 2007) and the sub-population of MK2 formerly bound to p38 is exported to the cytoplasm meeting its substrates such as Hsp25 and mRNA-binding proteins as tristetraprolin (TTP) (Hitti *et al*, 2006). Activated p38 may partially leave the nucleus (Ben-Levy *et al*, 1998), but also remains in the nucleus to phosphorylate transcription factors, such as ATF2 (Raingeaud *et al*, 1996) or MEF2 (Zhao *et al*, 1999), as well as PRC1-bound MK2/3. Activation of PRC-bound MK2/3 by p38 leads to phosphorylation of components of PRC1, such as Bmi1 (Voncken *et al*, 2005), and contributes to chromatin remodelling. Black balls symbolize phosphorylations.

activation of p38 MAPK under oxidative stress, which is probably paralleled by increased cytoplasmic accumulation of p38/MK2 complexes (Ben-Levy *et al*, 1998) and, hence, by their reduction at the PRC1, induces loss of 'stemness', similar to our findings in MK2-deficient mice. Thus, our analysis of MK2-deficient HSC may provide a missing link between the stress-induced MAPK pathway and Bmi1-controlled HSC maintenance.

It has been shown that the protein kinase MK3/3pK, which is closely related to MK2 and shows 75% identity in primary structure, is able to directly phosphorylate His-tagged Bmi1 *in vitro* at as yet unidentified sites (Voncken *et al*, 2005). In light of this observation, the MK2 could directly phosphorylate Bmi1 *in vivo*, as both enzymes share activators and substrates (Clifton *et al*, 1996; Ronkina *et al*, 2007).

Physiologically, we identified a new role for MK2 in maintaining HSC quiescence. Although we could show that the haematopoietic differentiation program seems to be intact in MK2-deficient cells, we identified a selective deficiency of the HSC compartment, as shown by decreased numbers of HSCs in MK2-deficient mice. Furthermore, we defined an increased fraction of proliferating cells in the early haematopoietic progenitor cell pool as well as increased *in vitro* proliferation, suggesting that MK2 is needed to put brakes on a state of quiescence by modulating the PRC1 complex. As a consequence of MK2 deficiency, 'stemness' is lost, as the